Co-funded by the

CEBAMA

➢ (Contract Number: 662147)

Deliverable n° D3.07

Final results and main outcomes of the Modelling Task

Editors: Andrés Idiart, Marcelo Laviña (Amphos 21)

Date of issue of this report: 08.03.2019

Report number of pages: 45

Start date of project: 01/06/2015 Duration: 48 Months

Project co-funded by the European Commission under the Euratom Research and Training Programme on Nuclear Energy within the Horizon 2020 Framework Programme		
Dissemination Level		
PU	Public	X
PP	Restricted to other programme participants (including the Commission Services)	
RE	Restricted to a group specified by the partners of the CEBAMA project	
CO	Confidential, only for partners of the CEBAMA project	

ABSTRACT

One of the goals of CEBAMA is to improve our understanding of interaction processes between cementitious and clayey materials. Different modelling approaches were used for modelling and interpretation of experimental data generated within Work Package 3 (WP3) of CEBAMA, with focus on reactive transport processes that can impact the physical properties of cementitious materials and their interface with clayey systems. Therefore, a common modelling task was conducted to build confidence in the consistency of the different modelling approaches. The work consisted in benchmarking the capabilities of various reactive transport codes to simulate physical and chemical processes governing long-term interactions at the concrete-clay interface. The goal of this task is also to cluster WP3 activities around a common simulation case and integrate the different spatial and temporal upscaling methods used by each partner. The work related with this activity has been undertaken during a period of nearly 2 years between 2017 and 2019. This report presents a detailed description of the Modelling Task and the main results obtained. The contents have been discussed and agreed between the different participating teams. A reference case was simulated using different reactive transport modelling tools, as well as a set of sensitivity cases for assessing the impact of numerical codes specificities, material variabilities, and uncertainties on the extent of alteration. The studied system considered a generic low-pH concrete structure in contact with a clayey host rock. A one-dimensional setup under fully saturated conditions was considered. The concrete composition corresponds to the low-pH concrete used in CEBAMA as an experimental benchmark. The composition of the clay host rock corresponds to the Callovo Oxfordian claystone. This study has served to build confidence in the representation of this complex system with reactive transport tools used within CEBAMA when simulating the long-term behaviour of low-pH cementitious systems. The results show not only the high level of understanding of the governing processes but also the good agreement obtained with different codes, which is essential to demonstrate the applicability of these numerical tools in safety assessments.

1 INTRODUCTION

Work Package 3 (WP3) on modelling and interpretation of experimental data gathers a total of 13 partners. The focus of the modelling work is mainly on reactive transport processes that can impact the physical properties of cementitious materials and their interface with clayey systems. However, diverse modelling approaches are used by each partner, focusing on different physical and chemical processes at several scales of analysis. A Modelling Task that aims at integrating the results and conclusions obtained by each partner is thus needed. The goal is to foster synergies between partners and present the outcomes of WP3 in a more structured way. This deliverable presents the main outcomes of the Modelling Task. The results in terms of concrete-clay interaction processes are discussed in detail and the results obtained using different numerical tools and simulation cases are compared.

A large body of literature is available about the modelling of cement-clay interactions. Reviews by Gaucher and Blanc (2006), Savage et al. (2007), and Bildstein and Claret (2015) are comprehensive studies of the level of knowledge and main uncertainties in this field. Most of the studies published in the past have focused on the clayey system, disregarding the interaction with a cementitious barrier (Savage et al., 2002; Gaucher et al., 2004; Lehikoinen, 2009; Watson et al., 2009; Fernández et al., 2010). In those studies, the cementitious system is typically replaced by a fixed concrete porewater as boundary condition. Marty et al. (2014) and Marty et al. (2015) presented a systematic study of the interaction between a Callovo-Oxfordian clay formation and a high-pH concrete. Other studies have focused on the prediction of the formation of an alkaline plume (e.g. Soler et al., 2011; Grandia et al., 2010; Sidborn et al., 2014), or the degradation of cementitious systems by clayey porewaters (Olmeda

et al., 2017). More recently, the simultaneous interaction between clayey and cement-based materials have been given more attention (Trotignon et al., 2006; De Windt et al., 2008; Marty et al., 2009; Kosakowski and Berner, 2013; Soler, 2013; Liu et al., 2014; Marty et al., 2014; Mon et al., 2017). The overall degradation sequence of "high-pH" OPC concrete is well-known (Miller et al., 2000; Marty et al., 2014; Olmeda et al., 20171). However, the interaction of low-pH concrete with clayey materials, as in the present work, has been given much less attention. Thus, the purpose of the Modelling Task is not only to build confidence in the modelling approaches with the benchmark exercise, but also to increase the level of understanding of the alteration of low-pH cementitious materials in contact with a clay system.

2 METHODOLOGY

An overview of the partners, modelling tools and simulated cases is presented here. A total of 8 partners from WP3 have been involved in the Modelling Task, as shown in Table 1. The reactive transport software used in the Modelling Task, also summarized in Table 1, are: iCP (Nardi et al., 2014), OpenGeoSys-GEM (Kosakowski and Watanabe, 2014), MIN3P (Mayer et al., 2002), CORE2D (Samper et al., 2011), and ORCHESTRA (Meeussen, 2003). Modelling Task related activities are presented in Table 2. Several cases (described in Table 3) of increasing complexity have been implemented and simulated. Table 4 presents a summary of the main processes considered in each case. The Modelling Task activities started at the 2nd Annual Workshop in May 2017, where the details of the simulation cases and the input data from characterization of the reference mixes in WP1 were set.

First results of the preliminary cases were discussed in the 3rd Annual Workshop. The final results and conclusions will be presented in the 4th Annual Workshop and are here described in more detail.

Table 1. *WP3 partners involved in the Modelling Task and numerical tools used.*

Nº	**Partner**	**Modelling tool**
1	AMPHOS 21 (A21)	iCP and PHAST
2	KIT	iCP
7	JUELICH	OGS (OpenGeoSys-GEM)
9	NRG	ORCHESTRA
14	UDC	CORE2D
23	PSI	OGS
24	ANDRA	MIN3P

Table 2. *Modelling Task related activities.*

Date	**Milestone**
January 2017	Deliverable D3.03. Consolidated plan for Upscaling Modelling Task
September 2017	WP1 data transfer on the CEBAMA reference mix
September 2017	Coordination meeting (Barcelona)
April 2018	Preliminary benchmark results of all teams at 3rd Annual Workshop, France
June 2018	Coordination meeting (Videoconference)
July 2018	Second WP1 and WP2 data transfer
October 2018	Poster and short presentation at NUWCEM 2018 conference, Avignon, France
February 2019	Final results of concrete/clay interface processes modelling
March 2019	Presentation of final results at the 4th Annual Workshop, Karlsruhe, Germany
May 2019	Joint paper in a peer-reviewed journal
June 2019	Poster at EURADWASTE 2019 conference, Pitesti, Romania

Table 3. *Description of the simulated cases and acronyms used.*

ID	Description
P1	Preliminary case 1: diffusion of a tracer from the concrete material to the bentonite
P2	Preliminary case 2: diffusion plus cation exchange and aqueous speciation reactions
P3	Preliminary case 3: diffusion plus cation exchange, aqueous speciation, and mineral reactions in equilibrium
FRC	Full Reference Case: full chemical description of the materials, including kinetics controlling the precipitation/dissolution of a list of minerals
S1	Sensitivity case 1: consideration of different porosity couplings (i.e. liquid phase amount, effective diffusion coefficient)
S2	Sensitivity case 2: effective diffusion coefficient in concrete is reduced by 1 order of magnitude
S3	Sensitivity case 3: electrochemical coupling (i.e. Nernst-Planck equations) is considered
S4	Sensitivity case 4: use of a different thermodynamic database

Table 4. *Simulation cases. TDB stands for thermodynamic database.*

	P1	P2	P3	FRC	S1	S2	S3	S4
Tracer diffusion	×	×	×	×	×	×	×	×
Aqueous species + cation exchange		×	×	×	×	×	×	×
Minerals in equilibrium			×	×	×	×	×	×
Reaction kinetics				×	×	×	×	×
Porosity couplings					×			
Lower diffusion in concrete						×		
Multicomponent diffusion							×	
Use of different or updated TDB								×

3 DESCRIPTION OF THE MODEL SET UP

The studied system considers a generic concrete structure in contact with a clayey host rock. Both materials are considered as homogeneous and continuous porous media. No excavation damage zone (EDZ) formation is considered in the conceptual model. The concrete structure has a thickness of 0.30 m and is surrounded by a large mass of clayey formation. In this context, a one-dimensional setup is proposed, with a clay thickness of 40 m. The geometry and boundary conditions considered in the model are shown in Figure 1 (Cartesian 1D). Isothermal (25 ºC) and fully water saturated conditions are considered in the model.

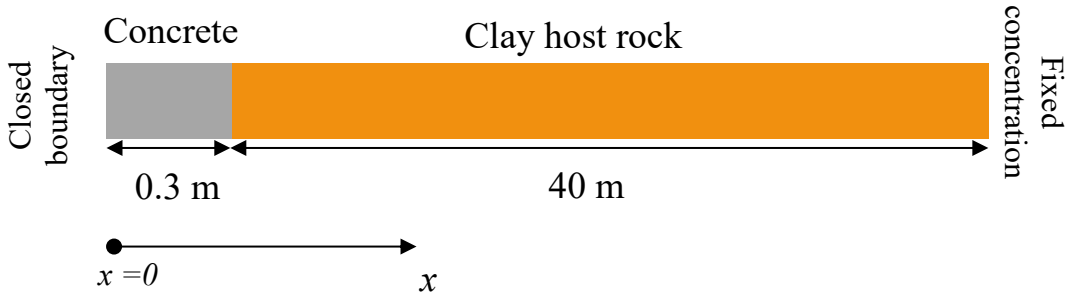

Figure 1. *Geometry and boundary conditions considered in the model. Fixed concentration (Dirichlet) at the clay boundary corresponds to fixed porewater composition equal to the initial composition in the clay (see Table 14).*

The concrete mineralogy and porewater composition correspond to a low-pH concrete, as described in Section 3.4. In WP1, low-pH cementitious materials have been proposed, referred to as CEBAMA reference mixes (e.g. Vehmas et al., 2016). Cement paste and concrete specimens were cast and distributed to interested partners. A relatively large dataset of experimental characterization of this reference mix has been obtained, both for the intact and aged states (Vehmas et al., 2018). Some experiments performed with this reference mix in WP1 have been in turn modelled and interpreted within CEBAMA. Therefore, the concrete mix considered in the Modelling Task corresponds to the CEBAMA reference concrete mix.

The composition of the clay host rock could in principle be any of the studied clayey materials within CEBAMA. In the Modelling Task, it was decided to consider the Callovo Oxfordian claystone (COx), as detailed in Section 3.5. One of the main reasons supporting this choice is the need of a well characterised clay rock to focus on the cementitious system. In this regard, the Callovo Oxfordian claystone has been considered in a recent benchmark study focusing on modelling interface evolution between a “high-pH” (ordinary Portland cement) concrete and COx (Marty et al., 2015).

This modelling task consists of a reference case and a set of sensitivity cases introducing new parameter values or integrating additional processes in the simulation setup (Table 4).

The reference case is divided into several steps with an increasing level of complexity of the processes considered in the simulation. These preliminary steps, modelled before performing the full reference case simulation, are also defined in Table 4.

3.1 Physical properties

For the COx claystone, the same parameters as in Marty et al. (2015) are used. Concerning the cementitious reference mix, porosity measurements using mercury intrusion porosimetry (MIP) indicate a total intruded porosity of between 0.023 and 0.038 for the reference concrete mix, referred to RCM (Vehmas et al., 2108). A porosity of 0.19 was measured using MIP (Vasconcelos et al., 2018) for the cement paste reference mix, referred to as RPM, corresponding to a concrete porosity of ~0.045 (assuming the same amount of aggregates and filler). Hydration modelling results presented in Section 3.4 indicate a porosity of a well hydrated concrete of ~0.06. Therefore, a value of 0.04 is proposed in the Modelling Task.

Solute transport is exclusively Fickian diffusion in the reference case. Therefore, a single diffusion coefficient needs to be defined for all species to maintain electroneutrality of the pore solution. Electrochemical coupling (i.e. Nernst-Planck equations) is considered only as a sensitivity case (S3). It is expected that the diffusion coefficient of a well-cured and low water-to-binder (w/b) ratio concrete mix as the one studied here (see Appendix B) is low, given the low values of porosity and permeability measured (Vehmas et al., 2018). The proposed effective diffusion coefficient value in the reference case is $1.00 \cdot 10^{-12}$ m^2/s. As a sensitivity case, it is proposed to use an effective diffusion coefficient in the lower range in case S2, with a value of $1.00 \cdot 10^{-13}$ m^2/s. This value is closer to the experimental results obtained for RPM samples using HTO (Vopálka et al., 2019). The porosity and the effective diffusion coefficient of the two domains are given in Table 5.

Table 5. *Physical properties of the clay and concrete domains considered in the model.*

Material	**Porosity**	**Pore diffusion coefficient (D_p, m^2/s)**	**Effective diffusion coefficient (D_e, m^2/s)**
COx claystone	0.18	$1.44 \cdot 10^{-10}$	$2.60 \cdot 10^{-11}$
Low-pH concrete	0.04	$2.50 \cdot 10^{-11}$	$1.00 \cdot 10^{-12}$

The reference case proposed in the Modelling Task does not consider diffusion-porosity coupling, i.e. changes in transport properties (D_e) as a result of chemical reactions and porosity variation. Feedback between chemical alteration and porosity and diffusivity is considered in a set of sensitivity cases (S1).

3.2 Time and space discretization

The spatial discretization is selected here as a compromise between the spatial resolution and the computation time for a given studied period. The studied period proposed is 100,000 years, although results are also compared at earlier times. According to the von Neumann criterion for diffusive solute transport, the time step size should comply with the following expression:

$$\Delta t < \frac{\Delta x^2}{3 \cdot D_p} \tag{3.1}$$

where t (s) is time, Δx is the spatial discretization (m), and D_p is the pore diffusivity (m^2/s). In this line, the proposed discretization is presented in Table 6. Given the higher pore diffusivity of the COx claystone compared to concrete, the time step size is restricted by the clay domain. Therefore, a finer discretization in the concrete domain (0 m < x < 0.3 m) can be used. This finer mesh is also adopted for the first 0.1 m of COx domain to avoid using elements of different size at both sides of the interface.

The temporal discretization considers a constant time step size of 0.10 years. Some of the codes used in this study have an automatic time stepping scheme. In those cases, a maximum time step size of 0.10 years has been used.

Table 6. *Spatial discretization used in the Modelling Task for each domain (concrete and COx).*

x (m)	Mesh/grid size (m)	Domain
0.0-0.3	0.02	Concrete
0.3-0.4	0.02	COx
0.4-1.8	0.04	COx
1.8-2.8	0.10	COx
2.8-7.8	0.50	COx
7.8-17.8	1.00	COx
17.8-37.8	2.00	COx
37.8-40.3	2.50	COx

3.3 Thermodynamic data

Several thermodynamic databases including different solids, minerals, and aqueous species, can be used to study either the cementitious system or the clay host rock chemical evolution. In the Modelling Task, the reference case considers the thermodynamic database ThermoChimie version 9b0 (Giffaut et al., 2014), which was updated at the end of 2015 with new data for clay minerals (Blanc et al., 2015) and available in different formats from https://www.thermochimie-tdb.com/. The version of ThermoChimie used assumes the extended Debye Hückel equation to calculate activity coefficients. The main reason to select this database is that it includes not only the cementitious system, but also the clay system and several radionuclides of interest. The impact of adding different thermodynamic data to ThermoChimie is assessed in a sensitivity case (S4), with new data available for cementitious phases from e.g. Roosz et al. (2018).

3.4 Low-pH concrete model

Characterization of the composition of the hardened concrete after curing requires the hydration of the mix to be modelled. Reactive transport models use the hydrated composition as an initial condition. The result of the hydration modelling includes the phase assemblage of the cement hydrates, the total porosity, and most importantly the porewater composition.

In the Modelling Task, the hydrated phase assemblage and porewater composition of the CEBAMA concrete reference mix is considered, corresponding to the results of the hydration model after 10 years of hydration (see Appendix A). That is, a fully-hydrated concrete is taken as initial condition for the long-term reactive transport calculations.

After 10 years of hydration, the amount of unhydrated clinker phases is extremely small and can be neglected, while the slag is completely dissolved. Therefore, only silica fume and quartz filler are considered in the simulations to kinetically dissolve. The kinetic parameters are presented in Table 7 and correspond to the pH-dependent kinetic dissolution of quartz given by Palandri and Kharaka (2004). Note that for quartz in the COx, a different kinetics of dissolution is used, corresponding to the one proposed by Marty et al. (2015). The reason to use a different kinetic rate is that for cement hydration calculations the rate in Marty et al. (2015) yielded a too slow dissolution of silica fume. The aggregates are considered as chemically inert, the same as with the superplasticizer.

Table 7. *Kinetic parameters for dissolution reactions in the concrete domain (from Palandri and Kharaka, 2004).*

Mineral	A **(m²/g)**	M_w **(g/mol)**	k_{25}^{nu} **(mol/m²s)**	k_{25}^{H+} **(mol/m²s)**	n^{H+}	θ	η
Quartz_filler	0.265	60.08	$3.98107 \cdot 10^{-14}$	$5.12861 \cdot 10^{-17}$	-0.5	1	1
SilicaFume	26.087	64.531	$3.98107 \cdot 10^{-14}$	$5.12861 \cdot 10^{-17}$	-0.5	1	1

As stated above, the silica fume and quartz filler dissolve under kinetically-controlled conditions. The reaction rate, r (mol/s), at 25ºC is given by the following expressions:

$$r = M_w \cdot m \cdot k \cdot A \cdot \left|1 - \Omega^{\theta}\right|^{\eta} \tag{3.2}$$

$$k = k_{25}^{nu} + \sum_i k_{25}^{i} \prod_j a_{ij}^{n_{ij}} \tag{3.3}$$

where M_w (g/mol) is the molar mass of the mineral, m is the total mass of the mineral (mol), k is the rate constant (mol/m^2/s), A (m^2/g) is the reactive surface area, Ω (-) is the mineral saturation ratio, θ and η are rate parameters (-), superscript *nu* refers to reactions under neutral conditions and superscript i to reactions under either acid or basic conditions, and a_{ij} is the activity of a species j in reaction i. Note that by performing the calculations at 25 ºC, the activation energy term is equal to 1 and is therefore not included here. Table 7 specifies the kinetic parameters for the quartz filler and silica fume. These parameters correspond to those for the quartz mineral from Palandri and Kharaka (2004), except for the surface areas, which are estimated from geometrical considerations (grain size distribution provided by the manufacturers of these materials).

The mineralogical composition of the low-pH concrete is given in Table 8, as well as the molar volumes (M_v, cm^3/mol) of the minerals for updating the solid volume. Besides mineralogical assemblage and porewater composition, the cementitious material is characterized by surface properties modelled through exchange processes. Table 9 specifies the composition of the cation exchanger in equilibrium with the pore solution that simulates the uptake of K and Na in the C-S-H (exchanged with Ca). The selectivity coefficients are based on the work by Missana et al. (2017) and on the use of the Gaines-Thomas convention. Uptake of aluminium in the cement hydrates is not considered in the model.

Table 10 presents the composition of the pore solution corresponding to the calculated porewater obtained in the hydration model after 10 years, including minor modifications, as explained below. The presence of redox sensitive species (i.e. iron, sulphur, chromium, etc.) in the cement mix might influence the redox potential of the cement porewater. For example, the presence of some species may cause the redox potentials to fall into the range -750 mV to -230mV in ordinary Portland cements (Berner, 2002). That is the case of sulphides in slag blends, or iron sorbed on C-S-H phases, substituting Al in AFm or AFt phases or precipitated as Ca-ferrites. With this in mind, and considering that total dissolved iron concentration does not exceed 10^{-7} M in cement pastes (Berner, 2002), a redox potential of ~ -27 mV has been taken into account, assuming a redox control by the thermodynamic equilibrium between magnetite/ferrihydrite couple at the given pH. Additionally, very low Cl and Sr concentration (10^{-10} M) are considered in the model to avoid numerical instabilities when assuming a value of 0. Finally, an inert tracer with a concentration of 10^{-3} M is added to the porewater to study solute transport in the system without the influence of chemical reactions.

The secondary minerals allowed to precipitate are listed in Table 11. Secondary minerals considered in the concrete domain are the same as those in the clay domain, see next section. This includes the

potential precipitation of illite under kinetic conditions, as well as quartz kinetic precipitation. For the later, the kinetics law defined for quartz in the COx domain is assumed.

Table 8. *Initial mineralogical composition of the low-pH concrete after hydration.*

Primary Minerals	mol/kg water	mol/L concrete	M_v (cm^3/mol)	Volume fraction (-)	Reaction type
CSH0.8	42.0055	1.68022	59.29	0.09962	Equilibrium
Calcite	0.2161	0.008644	36.93	0.00032	Equilibrium
Ettringite	0.2964	0.011856	710.32	0.00842	Equilibrium
Ferrihydrite(am)	1.6596	0.066384	34.36	0.00228	Equilibrium
Hydrotalcite	1.1709	0.046836	227.36	0.01065	Equilibrium
Magnetite	0.0005	0.000020	44.52	8.90E-07	Equilibrium
Stratlingite	1.1973	0.047892	215.63	0.01033	Equilibrium
Quartz_filler	43.7088	1.748352	22.69	0.03967	Dissolution kinetics
SilicaFume	12.4231	0.496924	28.06	0.01394	Dissolution kinetics
Inert solids*	-	-	-	0.77477	Inert
Porosity	-	-	-	0.040	

** Inert solids include the aggregates and superplasticizer volume fraction (see Table 18) and an additional solid volume needed to reach a porosity of 0.04*

Table 9. *Initial exchanger composition for alkali uptake in fully hydrated low pH-concrete and thermodynamic equilibrium constants (Gaines Thomas convention). CEC = cation exchange capacity.*

Exchanger	Log K	mol/kg water	mol/L concrete
Ex2Ca	0.0	$4.444 \cdot 10^{-01}$	$1.778 \cdot 10^{-02}$
Ex2K2	0.37	$5.524 \cdot 10^{-01}$	$2.210 \cdot 10^{-02}$
Ex2Na2	0.37	$1.689 \cdot 10^{-01}$	$6.756 \cdot 10^{-03}$
Total (CEC)		2.331	0.093

Table 10. *Initial porewater composition of the fully hydrated low-pH concrete.*

Variable	Value
pH	10.68
pe / (Eh)	-0.46 / (-27.2 mV)*
Totals	**Concentration (mol/kg water)**
Al	$1.448 \cdot 10^{-4}$
C	$1.506 \cdot 10^{-5}$
Ca	$5.237 \cdot 10^{-3}$
Cl	$1.000 \cdot 10^{-10}$
Fe	$5.447 \cdot 10^{-8}$
K	$3.420 \cdot 10^{-2}$
Mg	$3.736 \cdot 10^{-7}$
Na	$1.910 \cdot 10^{-2}$
S	$3.058 \cdot 10^{-2}$
Si	$2.021 \cdot 10^{-3}$
Sr	$1.000 \cdot 10^{-10}$
Tracer	$1.000 \cdot 10^{-3}$

** pe in equilibrium with Magnetite/Ferrihydrite(am) pair*

Table 11. *Secondary minerals considered in the low-pH concrete domain.*

Secondary Minerals	**M_v (cm^3/mol)**	**Reaction type**
Celestite	46.25	Equilibrium
Dolomite	64.3	Equilibrium
Pyrite	23.94	Equilibrium
Siderite	29.38	Equilibrium
Quartz	22.69	Precipitation kinetics
SiO_2(am)	29.00	Equilibrium
Brucite	24.63	Equilibrium
CSH1.6	84.68	Equilibrium
CSH1.2	71.95	Equilibrium
C3AH6	149.52	Equilibrium
C3FH6	154.50	Equilibrium
C4AH13	269.20	Equilibrium
C4FH13	274.4	Equilibrium
Ettringite-Fe	711.80	Equilibrium
Gypsum	74.69	Equilibrium
Hemicarboaluminate	569.02	Equilibrium
Hydrotalcite-CO_3	231.44	Equilibrium
$Fe(OH)_2$(cr)	24.48	Equilibrium
Monocarboaluminate	261.96	Equilibrium
Monosulfate-Fe	316.06	Equilibrium
Monosulfoaluminate	311.26	Equilibrium
Portlandite	33.06	Equilibrium
Pyrrhotite	18.20	Equilibrium
Saponite-FeCa	139.96	Equilibrium
Syngenite	151.63	Equilibrium

The elemental composition of the initial system in terms of chemical elements of the concrete domain, expressed in mol/litre medium, is summarized in Appendix B. This information is needed for some of the models to ensure a consistent setup of the initial system (e.g. for OGS and ORCHESTRA). Only the chemical elements included in the porewater, cation exchanger, and minerals in equilibrium are considered. The minerals that are kinetically constrained are not included but are reported separately in the same table.

3.5 Callovo-Oxfordian claystone model

The chemical model for the Callovo-Oxfordian claystone (COx) has been proposed by Andra within WP3 and is largely based on the work of Marty et al. (2015) and references therein. The model has been adapted to the ThermoChimie v9b0 database and incorporates two more species in the exchanger (Fe and Sr). The initial mineralogical composition of the COx is given in Table 12, as well as the molar volumes (M_v, cm^3/mol) of the minerals used for the update of solid volume and porosity. The exchanger composition and thermodynamic equilibrium constants are given in Table 13, Table 14 presents the equilibrated initial porewater composition.

Table 12. *Initial mineralogical composition in the claystone and molar volumes of the different minerals and secondary minerals considered in the entire domain.*

Primary Minerals	**M_v (cm^3/mol)**	**Reaction type**	**mol/kg_{water}**	**mol/L COx**
Porosity	-		-	0.18
Calcite	36.93	Equilibrium	27.9889	5.038
Celestite	46.25	Equilibrium	0.69	0.1242
Dolomite	64.3	Equilibrium	2.76	0.4968
Pyrite	23.94	Equilibrium	1.06	0.1908
Siderite	29.38	Equilibrium	1.10	0.198
Illite_Imt-2	139.18	Dissolution kinetics	10.77	1.9386
Montmorillonite-BCCa	132.48	Dissolution kinetics	2.75	0.495
Microcline	108.74	Dissolution kinetics	1.37	0.2466
Quartz	22.69	Precipitation kinetics	50.86	9.1548
Ripidolite_Cca-2	211.92	Dissolution kinetics	0.41	0.0738
SiO_2(am)	29.00	Equilibrium		
Brucite	24.63	Equilibrium		
CSH1.6	84.68	Equilibrium		
CSH1.2	71.95	Equilibrium		
CSH0.8	59.29	Equilibrium		
C3AH6	149.52	Equilibrium		
C3FH6	154.50	Equilibrium		
C4AH13	269.20	Equilibrium		
C4FH13	274.4	Equilibrium		
Ettringite	710.32	Equilibrium		
Ettringite-Fe	711.80	Equilibrium		
Ferrihydrite(am)	34.36	Equilibrium		
Gypsum	74.69	Equilibrium		
Hemicarboaluminate	569.02	Equilibrium		
Hydrotalcite	227.36	Equilibrium		
Hydrotalcite-CO_3	231.44	Equilibrium		
$Fe(OH)_2$(cr)	24.48	Equilibrium		
Magnetite	44.52	Equilibrium		
Monocarboaluminate	261.96	Equilibrium		
Monosulfate-Fe	316.06	Equilibrium		
Monosulfoaluminate	311.26	Equilibrium		
Portlandite	33.06	Equilibrium		
Pyrrhotite	18.20	Equilibrium		
Saponite-FeCa	139.96	Equilibrium		
Stratlingite	215.63	Equilibrium		
Syngenite	151.63	Equilibrium		

All minerals are considered under thermodynamic equilibrium, except for five kinetically-controlled minerals (Table 12). The kinetic parameters are given in Table 15 and Table 16. Among the kinetically controlled minerals, only quartz is allowed to precipitate (Table 16). Note that for quartz in the COx, different kinetic parameters of dissolution compared to those in concrete are used, corresponding to the one proposed by Marty et al. (2015). The reason to use a different kinetic rate is that for cement hydration calculations the rate in Marty et al. (2015) yielded a too slow dissolution of silica fume.

Table 13. *Initial exchanger composition in claystone and thermodynamic equilibrium constants following the Gaines Thomas convention. CEC = cation exchange capacity.*

Exchanger	Log K	mol/kg water	mol/L COx
Cox2Ca	0.7	$4.744 \cdot 10^{-01}$	$8.540 \cdot 10^{-02}$
Cox2Mg	0.7	$3.282 \cdot 10^{-01}$	$5.907 \cdot 10^{-02}$
CoxNa	0	$3.867 \cdot 10^{-01}$	$6.961 \cdot 10^{-02}$
CoxK	1.2	$7.850 \cdot 10^{-02}$	$1.413 \cdot 10^{-02}$
Cox2Sr	0.6	$1.188 \cdot 10^{-02}$	$2.139 \cdot 10^{-03}$
Cox2Fe	0.8	$2.860 \cdot 10^{-03}$	$5.145 \cdot 10^{-04}$
Total (CEC)		2.1	0.378

Table 14. *Initial porewater composition of the claystone.*

Variable	Value
pH	7.06
pe	-2.84
Totals	**Concentration (mol/kg water)**
Al	$8.504 \cdot 10^{-8}$
C	$3.826 \cdot 10^{-3}$
Ca	$7.601 \cdot 10^{-3}$
Cl	$4.120 \cdot 10^{-2}$
Fe	$4.351 \cdot 10^{-5}$
K	$5.110 \cdot 10^{-4}$
Mg	$5.187 \cdot 10^{-3}$
Na	$4.008 \cdot 10^{-2}$
S	$1.108 \cdot 10^{-2}$
Si	$1.800 \cdot 10^{-4}$
Sr	$2.429 \cdot 10^{-4}$
Tracer	0.000

Table 15. *Kinetic parameters for dissolution reactions in the COx domain (from Marty et al., 2015).*

Mineral	A (m^2/g)	k_{25}^{nu} (mol/m^2s)	k_{25}^{H+} (mol/m^2s)	n^{H+}	k_{25}^{OH-} (mol/m^2s)	n^{OH-}	θ	η
Illite_Imt-2	30	$3.3 \cdot 10^{-17}$	$9.8 \cdot 10^{-12}$	0.52	$3.1 \cdot 10^{-12}$	0.38	1	1
Montmorillonite-BCCa	8.5	$9.3 \cdot 10^{-15}$	$5.3 \cdot 10^{-11}$	0.69	$2.9 \cdot 10^{-12}$	0.34	0.17	10.34
Ripidolite_Cca-2	0.003	$6.4 \cdot 10^{-17}$	$8.2 \cdot 10^{-09}$	0.28	$6.9 \cdot 10^{-09}$	0.34	1	1
Microcline	0.11	$1.0 \cdot 10^{-14}$	$1.7 \cdot 10^{-11}$	0.27	$1.4 \cdot 10^{-10}$	0.35	0.09	2.35

Table 16. *Kinetic parameters for precipitation reactions.*

Mineral	A (m^2/g)	k_{25}^{nu} (mol/m^2s)	θ	η
Quartz	0.05	$3.0 \cdot 10^{-12}$	4.58	0.54

The elemental composition of the initial system in terms of chemical elements of the COx domain, expressed in mol/litre medium, is summarized in Appendix B. Only the chemical elements included in the porewater, cation exchanger, and minerals in equilibrium, are considered. The minerals that are kinetically constrained are reported separately in the same table.

3.6 Simplifications of reference case

Due to the complexity of the real system comprising the reactivity between concrete and clay materials, some simplifications are introduced in the conceptual model. Thus, compared to a real system, the reference case proposed in the previous sections owns some limitations, which can be refined with more sophisticated models, some of which are presented as sensitivity cases. Most of the simplifications considered are due to a lack of either experimental data and/or thermodynamic data. The main simplifications of the reference case are:

- No aluminium or magnesium uptake in C-S-H or other cement hydrates is considered;
- No solid solutions of C-S-H or aluminium-iron bearing phases are considered;
- Potassium and sodium uptake is modelled via cation exchange reactions;
- Iron in the initial concrete system is considered as ferrihydrite;
- Fickian diffusion is considered (electrochemical couplings are considered as a sensitivity case);
- Effective diffusion coefficient: two values are proposed (reference case and one sensitivity case) that were not experimentally determined but that are thought to well represent the concrete system,
- No coupling of porosity, aqueous mass, or diffusion coefficient, with chemical reactions is considered in the reference case. This is explored with several sensitivity cases.

Additionally, redox of the concrete system in the reference case is not expected to accurately represent real conditions in concrete, especially in this case where the addition of iron-rich blast furnace slag could significantly impact the redox potential.

3.7 Sensitivity cases

The list of four sensitivity cases is given in Table 4 and defined in more detail below. The results of the sensitivity cases are discussed in terms of differences with the reference case.

3.7.1 Porosity couplings (S1)

In the Full Reference Case (FRC), no coupling between porosity changes and transport properties is considered. Thus, the first sensitivity case, S1, considers the coupling between chemical reactions involving solid volume and porosity changes and ultimately the effective diffusion coefficient of the concrete and COx domains. To this end, several simulations with different porosity coupling schemes have been undertaken by five different partners (NRG, UDC, A21, PSI, and JUELICH).

Two different conceptual approximations have been considered: PSI and JUELICH restricted the level of coupling to the feedback between water volumetric content and the available porosity at each time step. Thus, liquid volume is scaled to the changing porosity, preserving volume balance. No coupling between porosity and the diffusion coefficient is considered. These models were implemented in OGS.

A second set of models take into account the effect of porosity changes due to mineral volume variations on the effective diffusion coefficient of concrete and clay. To this end, several simulations accounting for different relations between diffusivity and porosity have been performed.

The simplest expression used is the linear relation specified by equations (3.4) and (3.5), with ϕ representing porosity and D_p, the pore diffusivity, defined as a function of a constant tortuosity factor (τ) and diffusion coefficient in free water (D_w) by equation (3.4). The exponent (n) value for the linear relation is n=0. A sensitivity case with this linear diffusion-porosity law has been simulated by

A21, NRG, and UDC using iCP, ORCHESTRA, and CORE, respectively. A minimum porosity of 0.001 is set to prevent full clogging in any region of the modelled domain.

Alternative porosity-diffusion relations have also been used to study the impact of chemical alteration on the transport properties. These relations link total porosity changes to the diffusion coefficient using empirical expressions (e.g. Archie's law, exponential laws, etc.). Using Archie's law in equation (3.4), Andra, NRG, and UDC simulated concrete-clay interaction with an exponent value (n) equal to 1/3, while JUELICH used n=1.173. In turn, A21 has used the expression given by equation (3.6), where ϕ_0 is the initial porosity and $D_{e,0}$ is the initial effective diffusion coefficient (i.e., $1 \cdot 10^{-12}$ m^2/s in the FRC). Finally, JUELICH also considered another coupling, following equation (3.7). The model is based on a critical value for porosity (ϕ_c) (cf. Cochepin et al. 2008), fixed to be 70% of the initial porosity. A minimum value for effective diffusion coefficient ($1 \cdot 10^{-13}$) has also been defined in this simulation. Figure 2 shows the different porosity-diffusivity relations used, following equations (3.4), (3.5), (3.6), and (3.7) with different exponent values. It is noted that the constant tortuosity factor in equation (3.4) is defined on a case-by-case basis to match the initial pore diffusion coefficient value, depending on the value of exponent *n*.

$$D_p = \phi^n \cdot \tau \cdot D_w \tag{3.4}$$

$$D_e = D_p \cdot \phi \tag{3.5}$$

$$D_e = D_{e,0} \cdot \left(\frac{\phi}{\phi_0}\right)^{2.5} \tag{3.6}$$

$$D_e = D_{e,0} \cdot \left(\frac{\phi - \phi_c}{\phi_0 - \phi_c}\right)^{1.31} \tag{3.7}$$

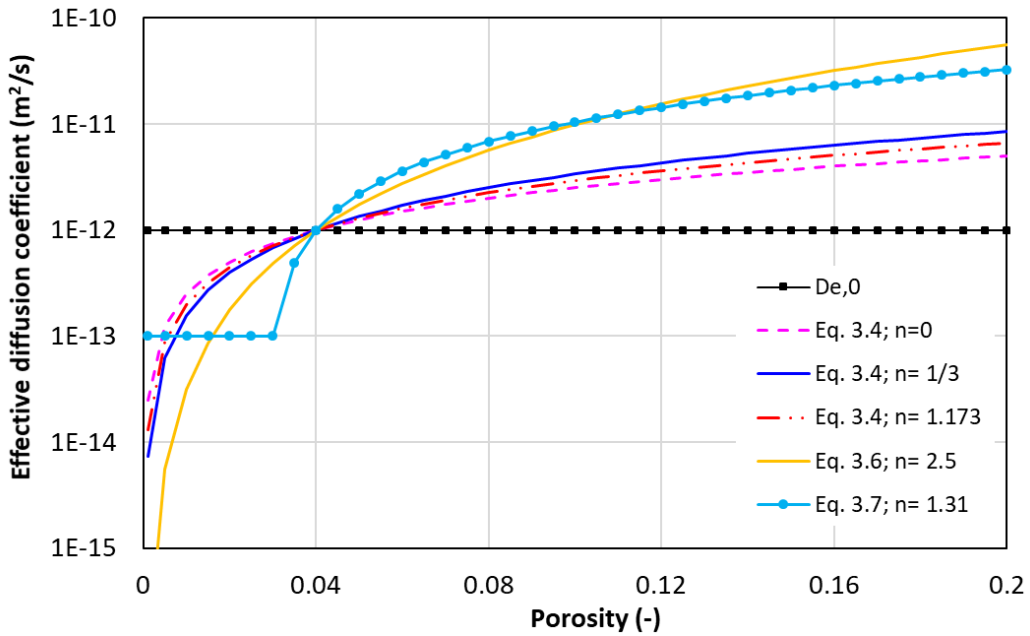

Figure 2. *Relations between porosity and effective diffusivity of concrete used in the models.*

3.7.2 Impact of the diffusion coefficient of the concrete domain

In this sensitivity case, a value of the effective diffusion coefficient of $1.0 \cdot 10^{-13}$ m^2/s has been considered. This value is expected to be more realistic for well hydrated conditions of the cementitious system, when compared to the value adopted in the reference case. The same simulation time (100,000 years), spatial discretization and time step size (0.1 years) as in the FRC are considered. The simulation was performed by Andra and UDC using MIN3P and CORE, respectively.

3.7.3 Impact of multicomponent diffusion

Multicomponent diffusion that includes the electrochemical coupling (i.e. Nernst-Planck equations) instead of Fick´s law has been considered as a sensitivity case. To compare with the reference case, the effective diffusion coefficient of neutral species is set to $1.0 \cdot 10^{-12}$ m^2/s. This sensitivity case has been performed by NRG with ORCHESTRA.

3.7.4 Impact of a different thermodynamic database on the results

In this sensitivity case, all chemical reactions have been simulated using ThermoChimie v9b0, as in the FRC, although an update of the database has been implemented according to new thermodynamic data compatible with ThermoChimie available from Roosz et al. (2018). Specific data for ternary blends and low-pH cementitious materials that have high aluminium oxide content are not currently available in ThermoChimie v9b and were added in this case, e.g. C-S-H with low Ca/Si ratio (0.6), and C-A-S-H and M-S-H phases. Davies equation, valid for the ionic strength of the studied system (<0.3 M) has been used. Polysulphides present in ThermoChimie have also been eliminated from the database. This sensitivity case was performed by KIT using iCP.

4 RESULTS

Simulation results are discussed and compared in terms of mineral phases, pore solution composition (totals, pH, ionic strength), exchanger composition and porosity. Code comparison is done based on the three preliminary cases and the Full Reference Case (FRC). In turn, the sensitivity cases are analysed by comparison with the FRC.

4.1 P1: Tracer diffusion (without considering geochemistry)

The diffusion of a non-reactive and uncharged tracer from the concrete domain towards the clay host rock in the setup presented in Figure 1 is shown here. Physical properties of the domains are those defined in Table 5, while the discretization is specified in Table 6. An initial tracer concentration in the concrete pore solution of 1 mM is considered, while the concentration is 0 in the COx. Boundary conditions are as shown in Figure 1 (closed boundary on the left and zero tracer concentration on the right). The results presented in Figure 3 show how the diffusion of the tracer towards the clay domain has the effect of decreasing its concentration in the concrete domain as a function of time. Good comparison between six codes is found for the tracer diffusion. An additional code has been used by A21 for this exercise, namely the reactive transport code PHAST (Parkhurst et al., 2010). After 100 years, small differences can be found, with lower concentrations predicted by MIN3P in the concrete domain. A slightly smaller initial mass of tracer in that simulation could be the reason for that difference (in MIN3P, the initial concentration is the same, i.e. $1 \cdot 10^{-3}$ M, although the mass of tracer initially extends over 29 cm instead of 30 cm).

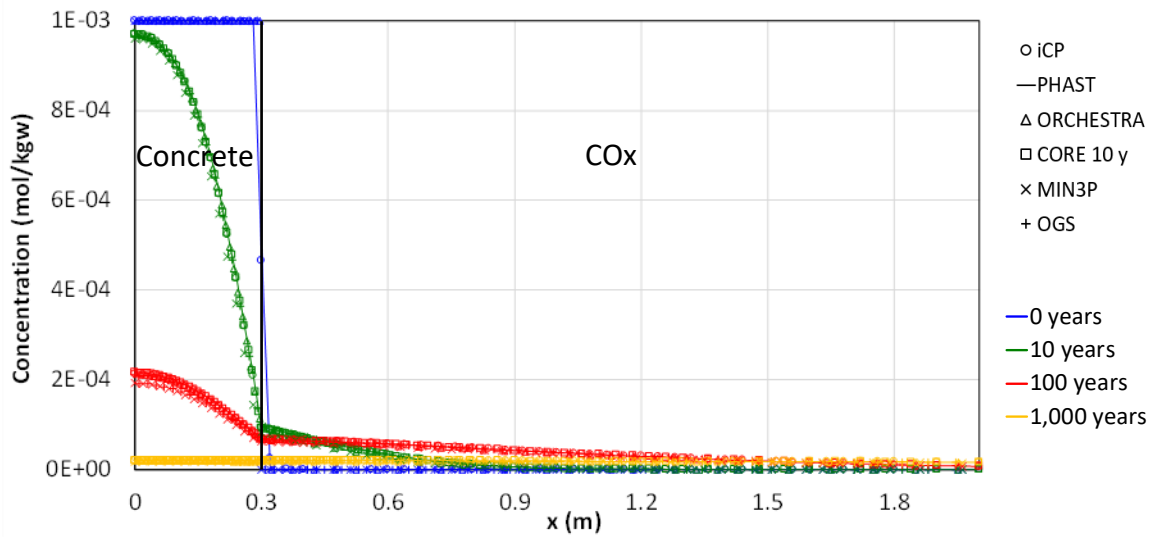

Figure 3. *Comparison of tracer concentration profiles (mol/kg water) at 0, 10, 100 and 1,000 years obtained with iCP, PHAST, ORCHESTRA, CORE, MIN3P and OGS. Only the first 2.1 m are shown (P1: Tracer diffusion).*

4.2 P2: Aqueous species and cation exchange

The setup of case P2 is equivalent to the one described for the FRC but without any primary or secondary mineral phase. Only the aqueous solutions and the cations in the exchanger of each material are considered. Thus, chemical interaction between concrete and clay is limited to the diffusion of their porewater solutions and interaction with exchangeable cations in local equilibrium with the

corresponding material. Results after 1,000 years of interaction are presented from Figure 4 to Figure 6. Results are centred on the first meter of the entire system, focused on the concrete-clay interface. The remaining COx domain (not-shown) presents flat distribution profiles of the different variables.

Cation (Ca^{2+}, K^+ and Na^+) concentrations at 1,000 years in concrete exchanger are presented in Figure 4. Initial concentrations are 0.45 mol/L, 0.55 mol/L and 0.17 mol/L for Ca^{2+}, K^+ and Na^+, respectively. At the left-most node (less degraded) Ca^{2+} concentration remains unchanged, while a K^+ reduction of 0.1 mol/L in favour of Na^+ is observed. Closer to the clay interface, K^+ concentration decreases as it diffuses towards the clay. Na^+ and Ca^{2+} concentrations increase towards the clayey side maintaining a similar Ca/Na ratio in the concrete exchanger. Good agreement between codes is shown, with slight differences in the case of MIN3P results. In turn, Figure 5 shows the composition of the first left meter of the clay exchanger. Potassium diffusion from concrete results in an important concentration increase in the clay exchanger. As a consequence, all other cation concentrations are reduced.

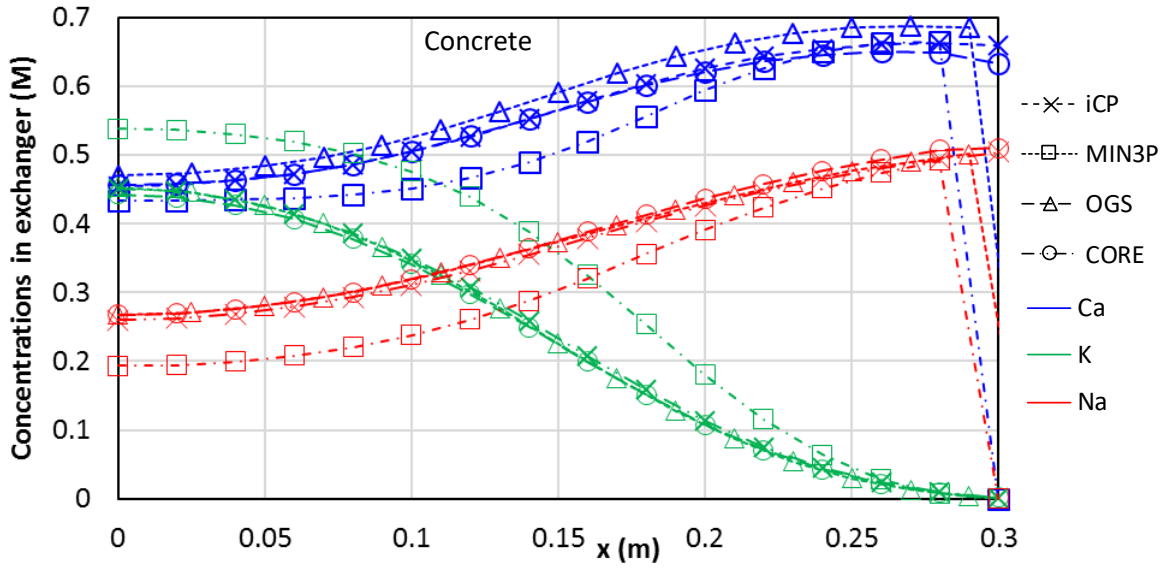

Figure 4. *Cation concentration (M) profiles in concrete exchanger at 1,000 years obtained with iCP, MIN3P, OGS and CORE (P2: aqueous species plus cation exchange).*

The distribution of aqueous species in the system is illustrated by total Ca and K profiles at 1,000 years in Figure 6. A flat pH profile (Figure 6) is shown after 1,000 years of interaction, with values between 7.1 and 7.2 for the two materials (initial pH values are 10.68 and 7.06 for concrete and clay, respectively). As the clayey domain is much larger (~130 times) than the concrete one, pH in the system tends to the initial values in the clay. Differences in porewater between codes can be directly linked with the differences observed in the exchanger compositions.

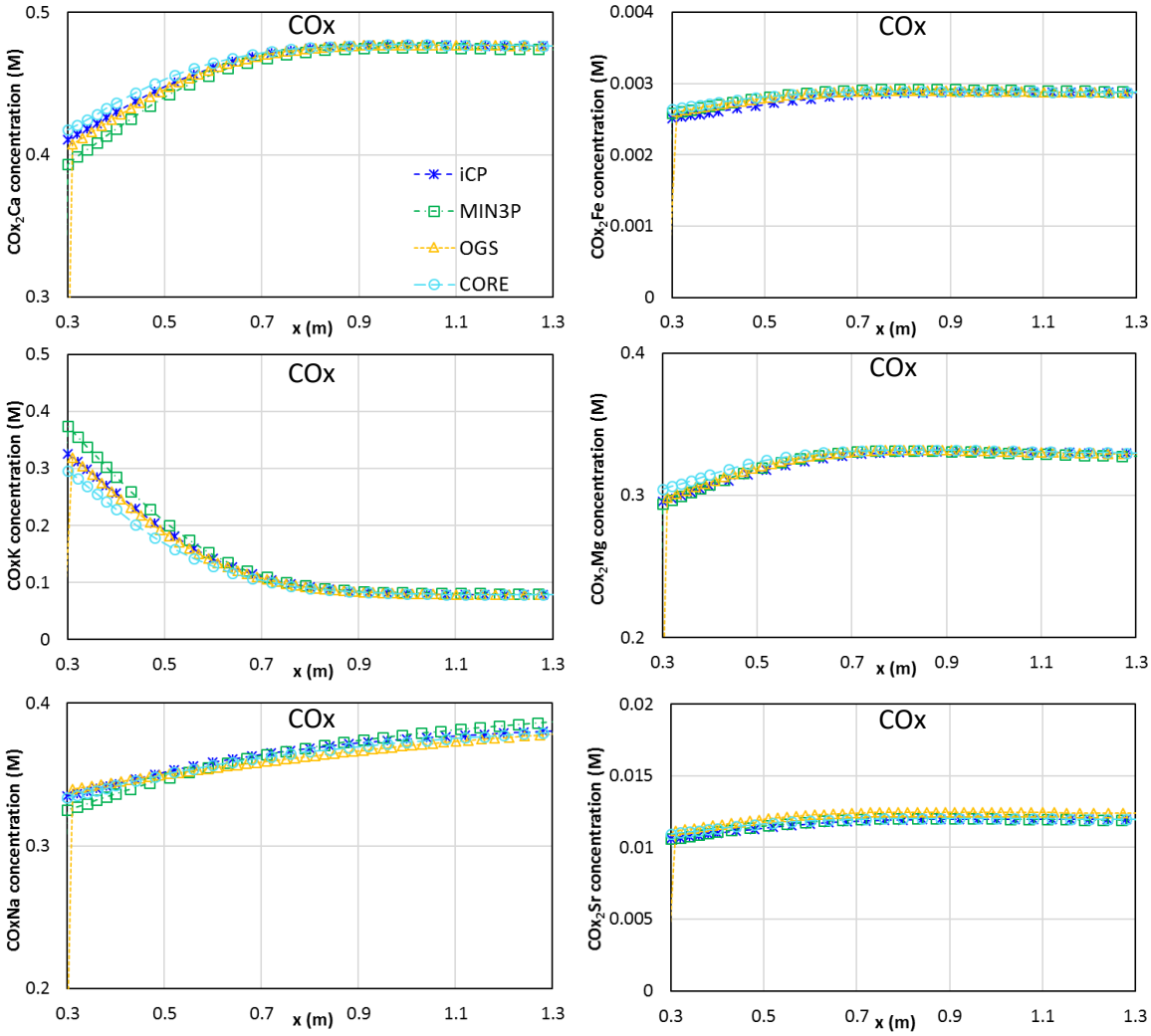

Figure 5. *Cation concentration (M) profiles in COx exchanger at 1,000 years obtained with iCP, MIN3P, OGS and CORE (P2: aqueous species plus cation exchange).*

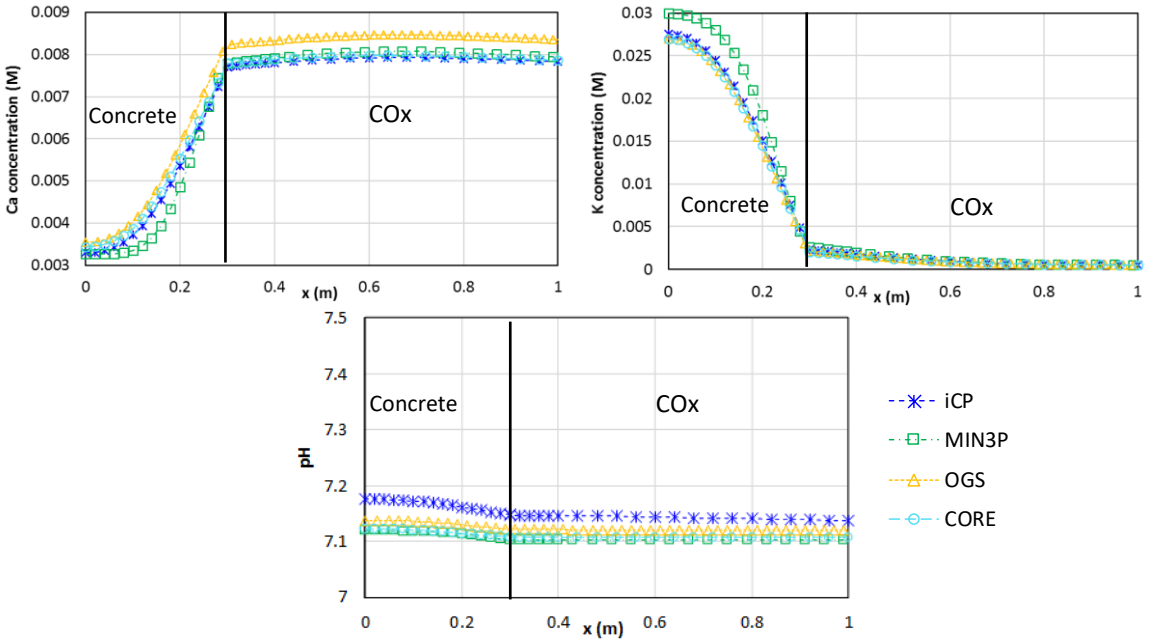

Figure 6. *Total aqueous concentrations (M) and pH profiles at 1,000 years E (case P2).*

4.3 P3: Minerals in equilibrium

The setup of Preliminary case 3 is equivalent to the FRC but without accounting for those minerals whose precipitation/dissolution is kinetically controlled. As an exception, quartz, although considered as kinetically controlled in the FRC, is included in P3 case as secondary phase in equilibrium in both materials. Quartz is expected to form in the model when the C-S-H gel is dissolved. In MIN3P, mineral reactions can only be simulated using kinetic rates. Thus, fast reaction kinetic rates ($1 \cdot 10^{-9}$ mol/L_{medium}/s) were considered to simulate thermodynamic equilibrium conditions. An overview of the results after 100,000 years is presented in terms of pH and porosity in Figure 7. Mineral profiles of interest at this same time are shown in Figure 8 and Figure 9.

The pH profile is a good indicator of chemical alteration. On the concrete side, alteration gradually increases when approaching to the clay interface (right axis on Figure 7). Maximum values (10.5) are shown in the innermost 16 cm, where C-S-H gel is still present. The decrease from the initial value is due to alkali (K) release to the clay. The profile slightly decreases from that point to x=22 cm, and then rapidly drops to reach a value of ~7.26 at the interface. On the COx side, pH alteration is much more reduced in magnitude, with a maximum increase at the interface of ~0.2 pH units. However, it extends nearly in the entire domain (40 m).

Porosity profile (left axis on Figure 7) is a result of the mineralogical alteration. It is noted that the porosity values presented for this case are not considered in the calculations to change the solid volume. Thus, no coupling with transport properties or water mass are taken into account. On the concrete side, initial values remain unaltered at the first 5 cm. As the degradation front approaches, an increase in porosity is shown, with values of ~0.1 between x = 15 cm and x = 0.22 cm. As degradation proceeds, porosity decreases mainly due to calcite precipitation. Negative values are predicted near the interface, indicating porosity clogging. On the clay side, porosity decreases in the 0.5 m next to the interface, although noticeable changes are only predicted for the closest 3 to 7 cm (values around 0.12 at the interface). In terms of code comparison, very small differences appear both in the pH and porosity profiles predicted by the different codes.

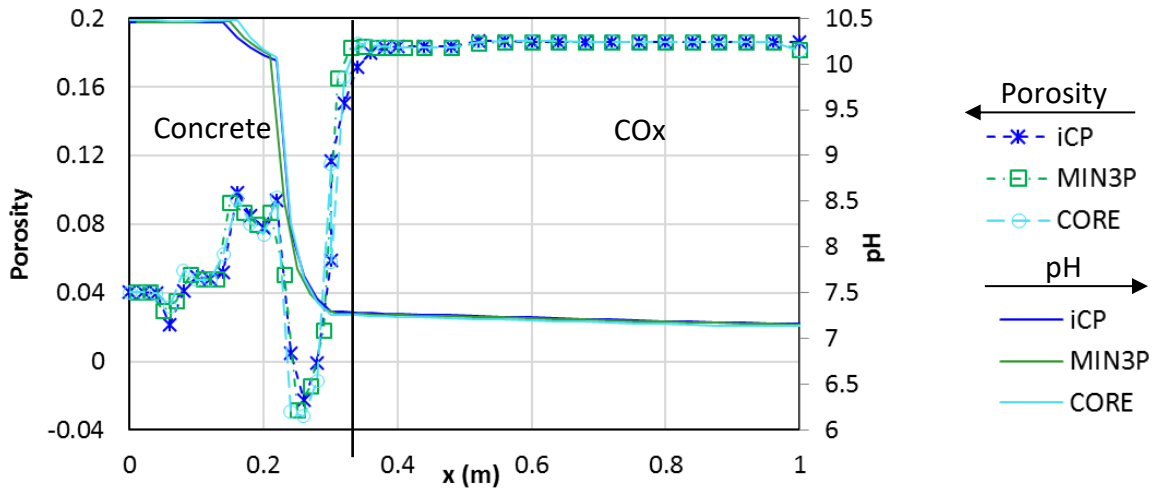

Figure 7. *Porosity and pH distribution profiles at 100,000 years obtained with iCP, MIN3P and CORE (P3: minerals in equilibrium).*

Figure 8 and Figure 9 present the distribution profiles of mineral phases after 100,000 years of interaction. The mineral degradation sequence is consistent with previous studies (e.g. Gaucher and Blanc, 2006; Savage, 2011; Marty et al., 2015). The main reactions in the concrete material include dissolution of C-S-H 0.8, ettringite, ferrihydrite, hydrotalcite and strätlingite. For hydrotalcite and

ettringite, there is a depleted zone next to the interface and a reprecipitation zone at the degradation front (Figure 8). Secondary phases in concrete are mainly brucite and, at lower concentration, saponite. Quartz, magnetite, celestite and calcite precipitate at both sides of the interface. Calcite is the main responsible for porosity clogging in concrete. Degradation in the clay domain is visible in the dolomite and siderite concentration profiles (Figure 9). Dolomite is depleted in the first 20 cm near the interface, while slightly dissolved in the next 60 cm. In turn, siderite completely dissolves in the first 1.1 m, triggering pyrite and magnetite precipitation. Overall, if C-S-H gel and dolomite depletion are taken as reference for concrete and COx degradation fronts, respectively, concrete degradation extends over half of its thickness (15 cm), while in the clay the front is at 20 cm. Overall, there is good agreement between the results obtained with the different codes. However, the sensitivity of the system to iron is visible, especially in the siderite and magnetite profiles.

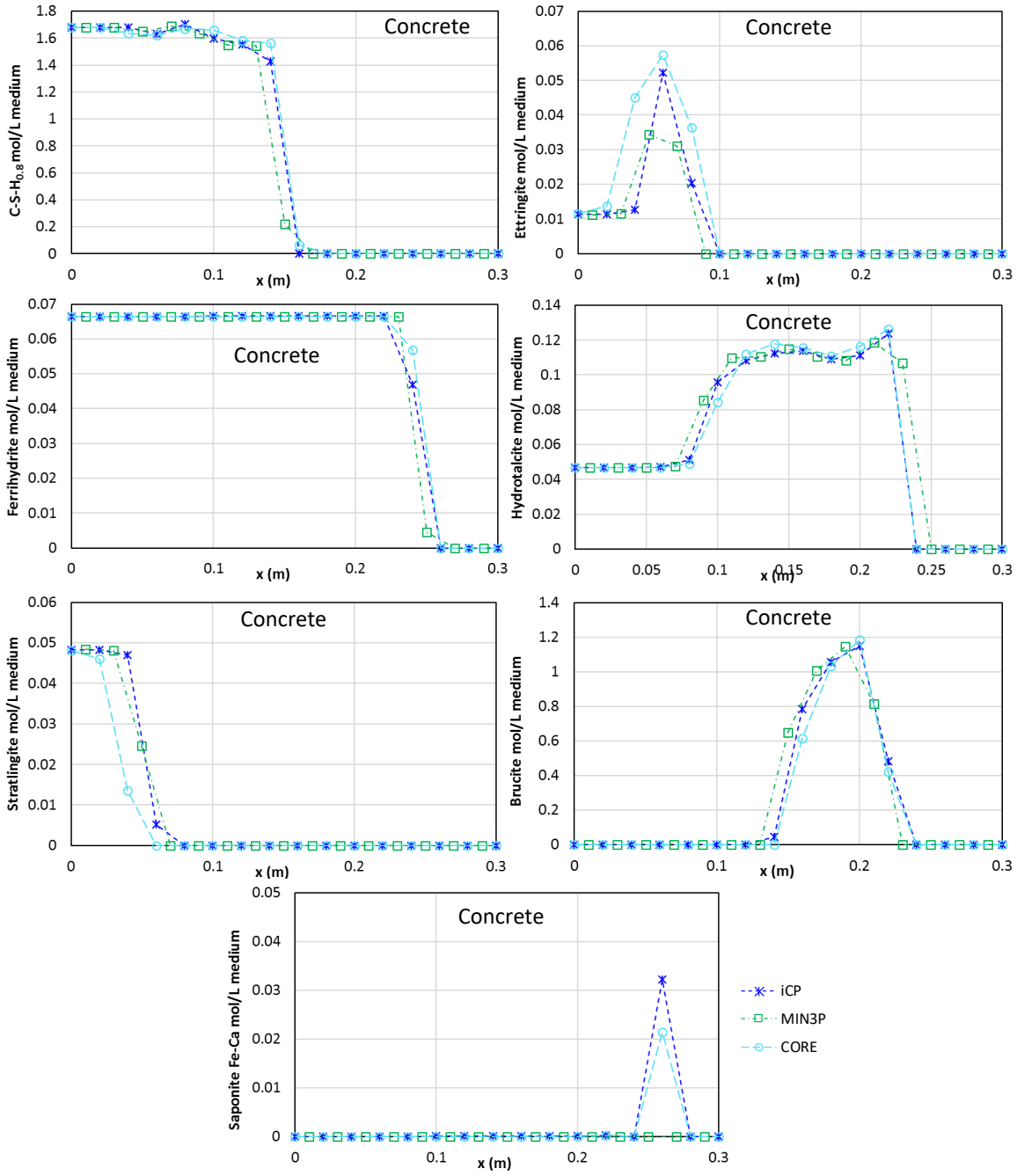

Figure 8. *Mineral phases profiles (in mol/ L medium) in the concrete domain at 100,000 years, obtained with iCP, MIN3P and CORE (P3: minerals in equilibrium).*

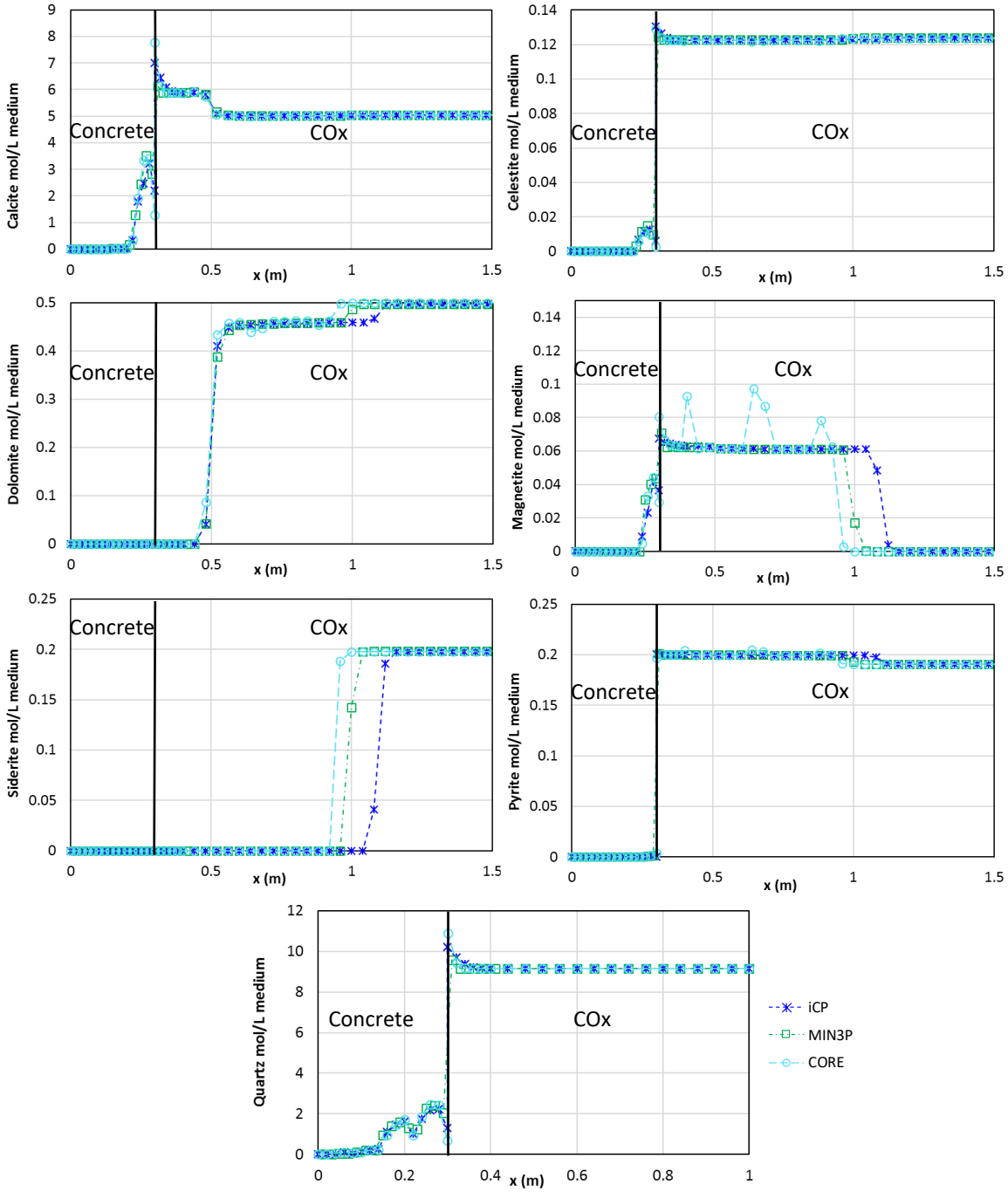

Figure 9. *Mineral phases profiles (in mol/ L medium) in concrete and clay domains at 100,000 years, obtained with iCP, MIN3P and CORE (P3: minerals in equilibrium).*

4.4 FRC: Full reference case

The reference simulation of the Modelling Task is named the Full Reference Case (FRC). As described in Section 3, this case includes cation exchange reactions and dissolution/precipitation of mineral phases in equilibrium and/or kinetically controlled. On the other hand, no coupling between solid volume changes and solute transport is considered. The results are presented and compared here by means of distribution profiles after 100,000 years of concrete-clay interaction.

Figure 10 presents the aqueous concentration profiles at 100,000 years. Some species present important concentration gradients between concrete and clay porewaters, governed by equilibrium with different sets of minerals. On the other hand, other species show little variations (Cl, K, Na, S and Sr) due to the null or limited role in solid-liquid interaction. Concentration gradients are a result not only of mineralogical phase assemblages in each domain, but also cation distribution in the exchangers. Due to the complexity of the system, it is not easy to clearly identify direct links between all aqueous concentrations and mineral phases. As an example, aluminium decrease in the centre part of the concrete domain is a direct consequence of hydrotalcite reprecipitation in that region (see Figure 13). pH values after 100,000 years present a maximum value of 10.5 (13 cm in concrete), where C-S-H gel is still present, while it decreases linearly to 10 at x=21 cm and then fall under 7.5 towards the interface. On the COx side, pH is around 7.3 at the interface and decreases to its initial value towards the right boundary.

Concrete exchanger composition is presented in Figure 11 in terms of cation concentration profiles at 100,000 years. Similar to the results obtained in P2, K^+ decreased to $\sim 10^{-4}$ M, while Ca^{2+} and Na^+ increased. Similar Ca^{2+} and Na^+ concentrations are predicted close to the interface. Figure 12 presents the distribution of cations in the clay exchanger at 100,000 years. The perturbation from the interaction with concrete is noticeable even far from the interface. Sr concentration presents slightly lower values than the initial ones in the first ~10 m, while an increase is observed close to the interface. The main cation exchange evolution observed in the clay is the increase in K^+ as it is leached from concrete. In turn, concentration of all other cations (except for Sr) decreases. This is in agreement with the results of Marty et al. (2015) for a high-pH concrete – COx interface.

The evolution of mineral phases in concrete is presented in Figure 13. Concrete degradation follows the expected sequence (e.g. Gaucher and Blanc, 2006; Savage, 2011; Marty et al., 2015). pH decreases first due to the leaching of alkalis and remains at ~10.5, in equilibrium with C-S-H 0.8. C-S-H 0.8 dissolves over half of the concrete domain (15 cm), triggering quartz precipitation due to release of Si. Dissolution of strätlingite, ferrihydrite, hydrotalcite, and ettringite is also observed. The latter two minerals reprecipitate over their initial values before being depleted. The two kinetically controlled primary mineral phases (quartz filler and silica fume) locally dissolve at around x= 23 cm. Phases precipitating in concrete are: brucite, Fe-Ca saponite, calcite, celestite, magnetite and quartz. These minerals also form on the clay side of the interface, except for brucite and Fe-Ca saponite. In terms of mineral volume (not shown), calcite precipitation is the most important mineral, being the main responsible for porosity clogging in concrete (Figure 14). Farther from the interface (from x= 15 cm to x= 22 cm), porosity values increase to ~0.1 and remain almost unaffected in the inner half (Figure 14).

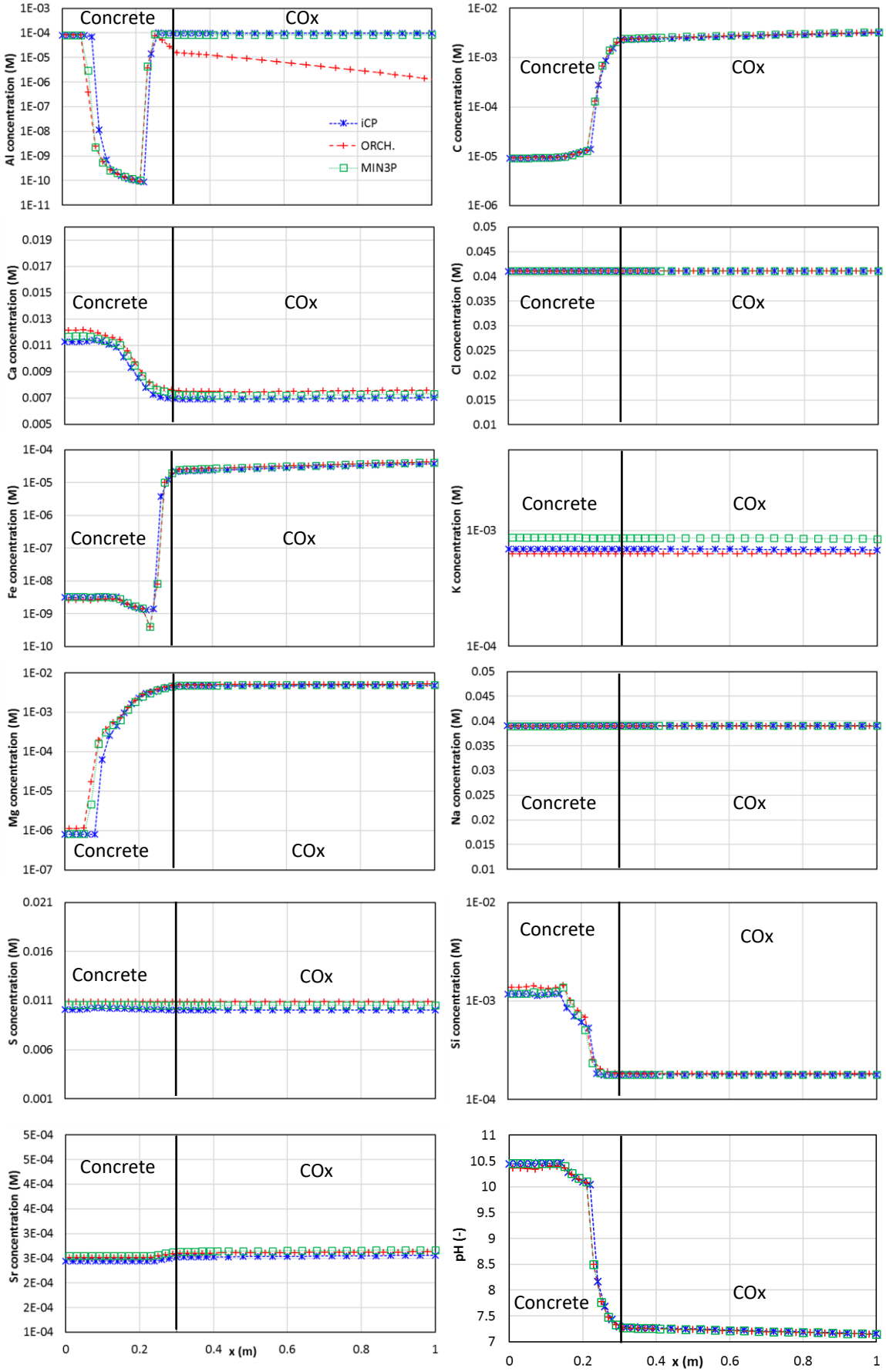

Figure 10. *Total aqueous species concentration (M) and pH profiles at 100,000 years obtained with iCP, ORCHESTRA and MIN3P (FRC: full reference case).*

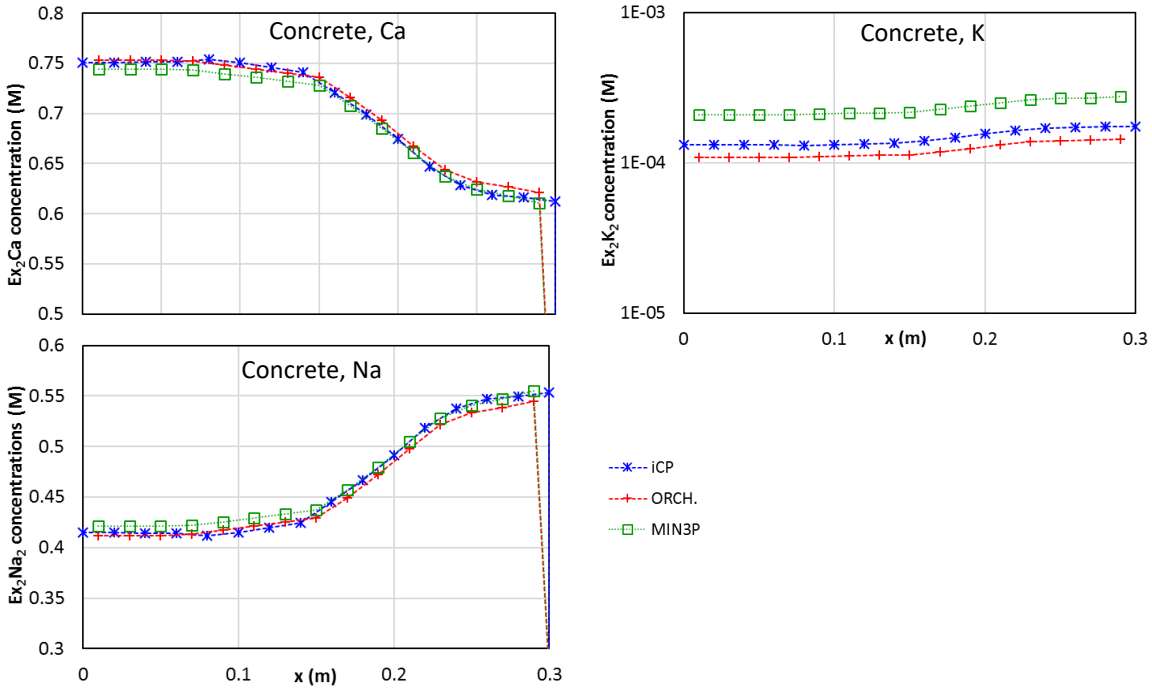

Figure 11. *Cation concentration (M) profiles in concrete exchanger at 100,000 years obtained with iCP, ORCHESTRA and MIN3P (FRC: full reference case).*

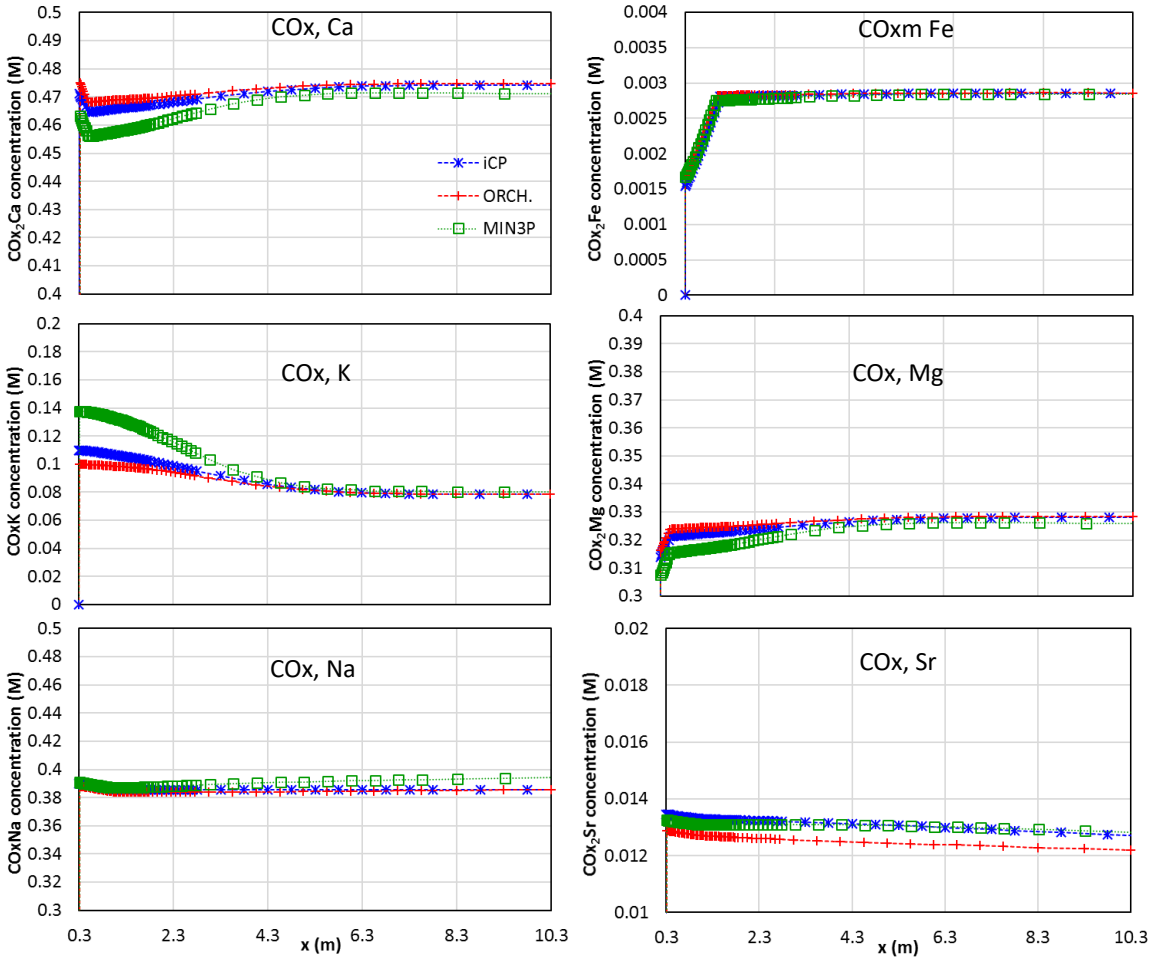

Figure 12. *Cation concentration (M) profiles in clay exchanger at 100,000 years obtained with iCP, ORCHESTRA and MIN3P (FRC: full reference case).*

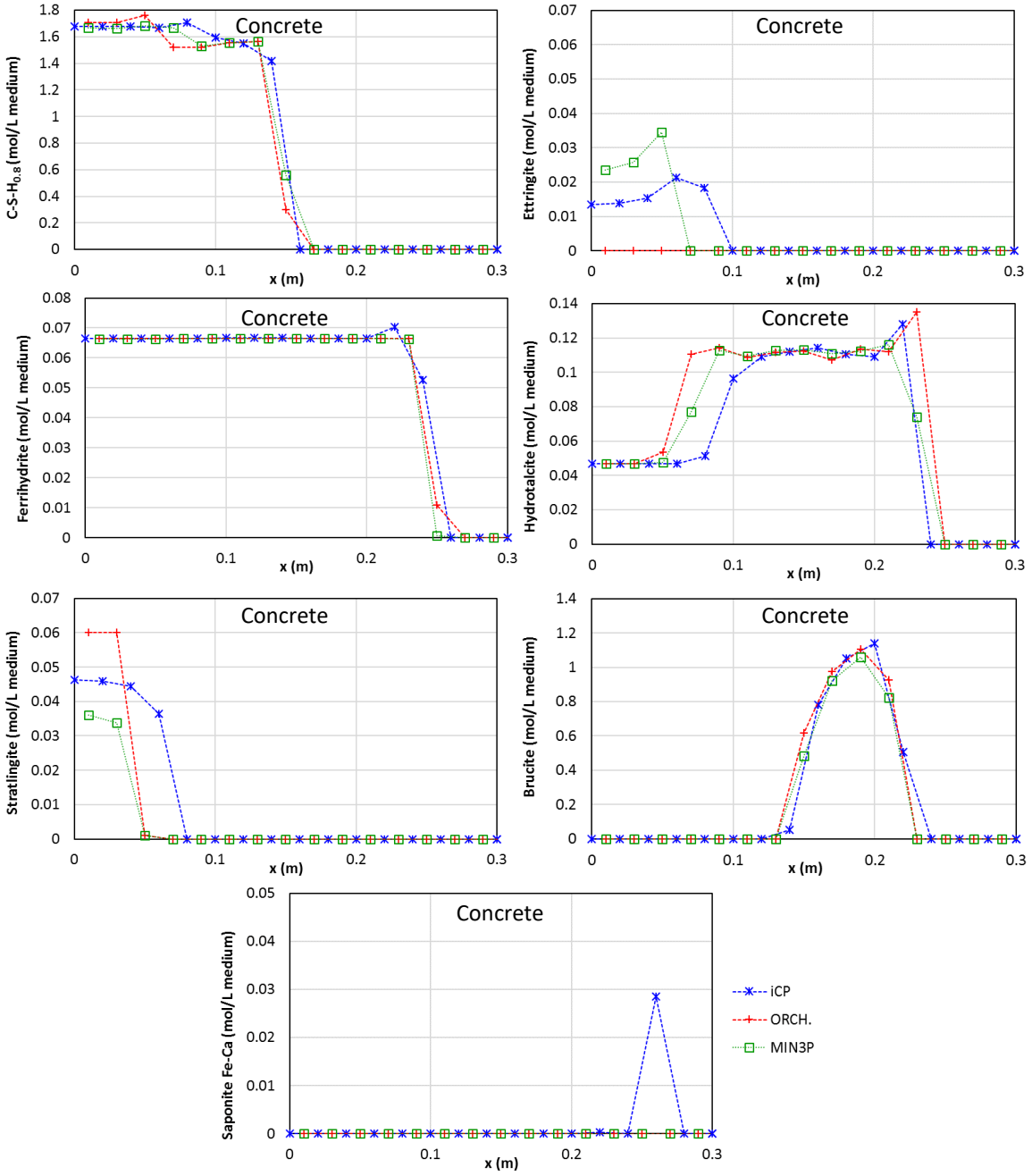

Figure 13. *Mineral phases profiles (in mol/ L medium) in the concrete domain at 100,000 years, obtained with iCP, ORCHESTRA and MIN3P (FRC: full reference case).*

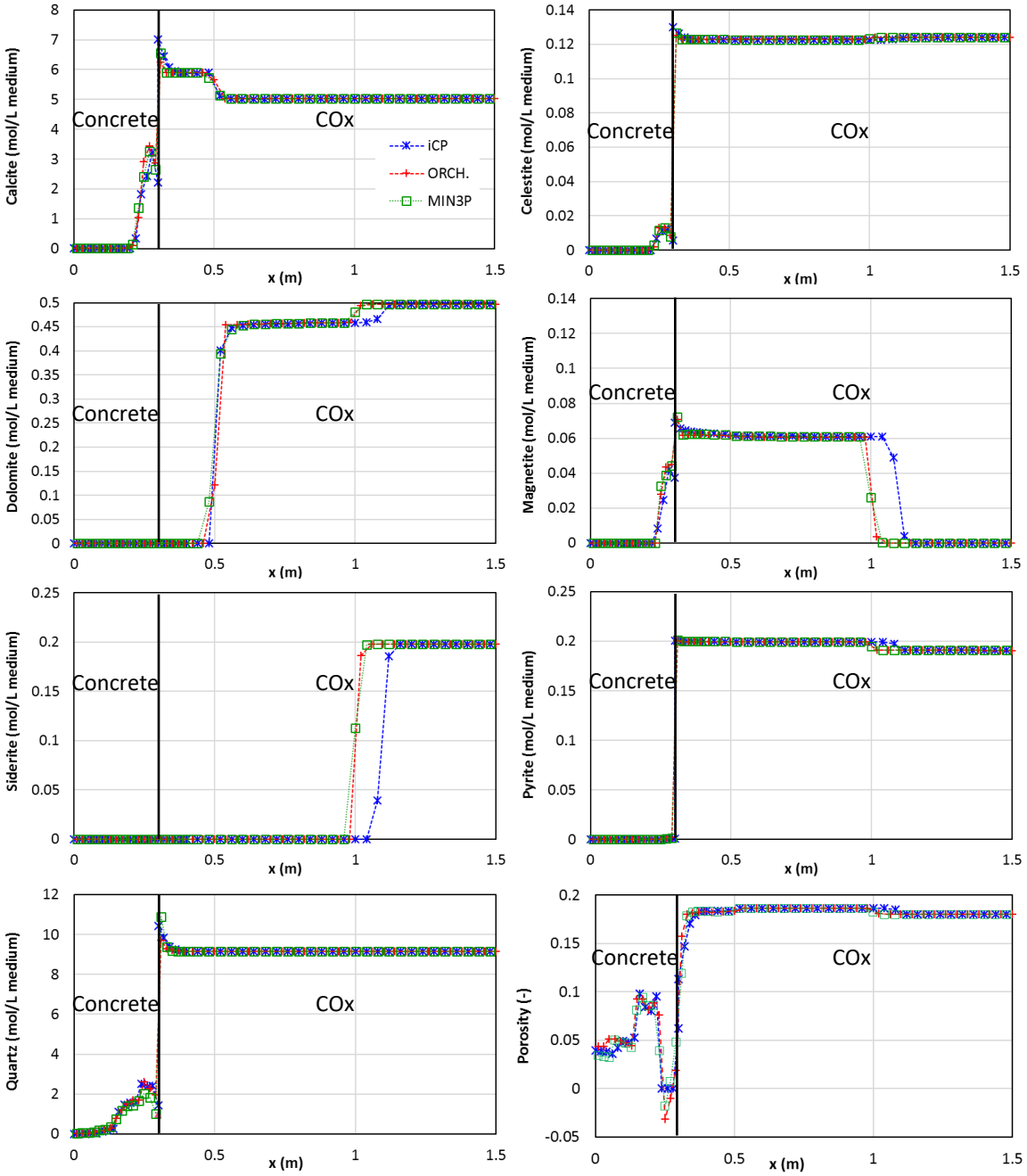

Figure 14. *Mineral phases (in mol/ L medium) and porosity (-) profiles in concrete and clay domains at 100,000 years, obtained with iCP, ORCHESTRA and MIN3P (FRC: full reference case).*

In turn, the mineralogical alteration of the clay is characterized by dolomite depletion in the first 20 cm from the interface and a slight concentration decrease in the next 80 cm (Figure 14). The dissolution front of siderite reaches a depth of 1-meter, favouring magnetite and pyrite precipitation. Montmorillonite and illite concentrations remain unchanged after 100,000 years of interaction with the low-pH concrete. This can be explained by the very slow dissolution kinetics at pH values smaller than 10.5. Porosity of the clay next to the interface decreases to ~0.1.

Overall, the results of the FRC are very similar to that obtained in P3 (with minerals in equilibrium only, Section 4.3). Thus, including kinetically-controlled mineral phases is, for this particular case, not a key factor. Primary kinetically-controlled minerals in the clay (montmorillonite, illite,

microcline and ripidolite) remain unaffected for 100,000 years. In concrete, silica fume and quartz filler are only dissolving very locally and are replaced by quartz precipitation. It is noted that quartz precipitation is considered here under thermodynamic equilibrium, which may be limiting the differences between P3 and FRC.

In terms of code comparison, results obtained with the different codes for mineral concentration profiles are in good agreement, especially for concrete degradation. In the clay domain, dolomite dissolution fronts agree well between different codes, while mineral profiles show some differences when comparing iron-based minerals (magnetite, siderite and pyrite).

4.5 S1: Porosity couplings

A set of sensitivity cases considered the effect of mineral precipitation/dissolution on the transport properties (porosity and diffusion coefficient). The couplings used in each model differ among partners. Code comparison is thus not the objective of this sensitivity case, but to assess the impact of the coupling of porosity changes on the results of the FRC. Two main variables are selected as key indicators: (1) porosity, which reflects the mineralogical evolution, and (2) pH, as it is a good indicator of chemical alteration in the analysed materials.

First, the models that scale the liquid phase volume with porosity changes (volume balanced) are presented and compared to the results of the FRC. Figure 15 presents the distribution profiles of porosity and pH at 100,000 years. The results of the overall degradation process are similar to those of the FRC, although higher maximum values for porosity are predicted, while pH values in the inner concrete region are lower than those of the FRC. The largest differences are found in the cation concentrations in the concrete exchanger (Figure 15), as the concentrations in these two S1 models are referred to updated water mass values (while referred to initial water mass in the FRC). Liquid phase volume decreases with porosity and at $x \approx 0.25$ m the reduction is significant. This results in high cation concentrations in the exchanger (around 6 mol/L medium). Mineral distribution profiles in concrete are similar to those obtained for the FRC (Figure 15). Differences at the interface are probably due to the different numerical approaches in the different codes. For instance, calcite concentration at the interface is an average value between concrete and clay values for OGS, while in iCP the value for the concrete domain is different to that of the clay domain at the interface.

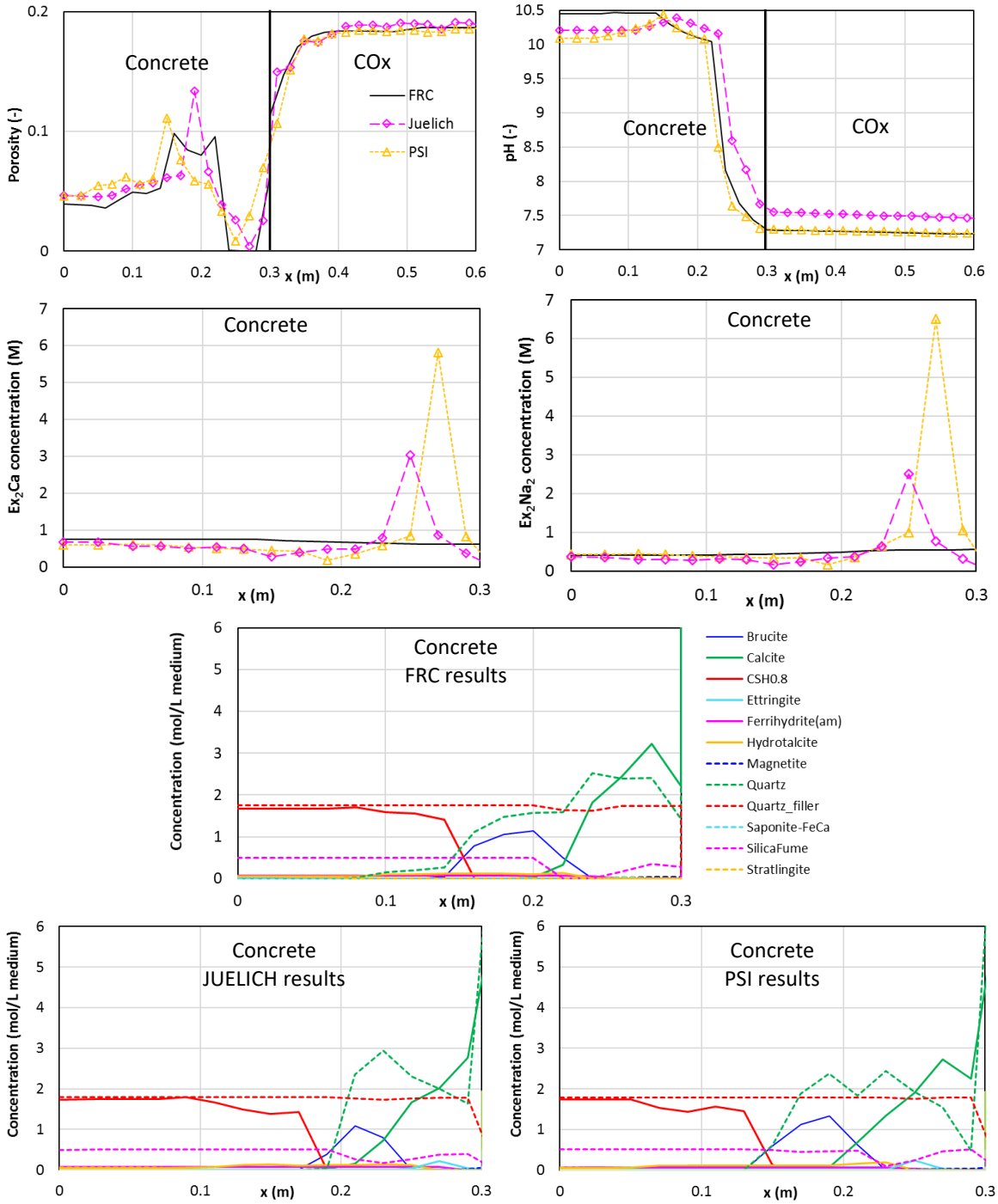

Figure 15. *Porosity (-), pH (-) and cation concentration (M) in concrete exchanger distribution profiles at 100,000 years. Results for FRC and models coupling porosity with liquid phase developed in PSI and JUELICH (S1: porosity coupling).*

The second set of simulations considering porosity coupling is based on affecting the effective diffusion coefficient linearly with porosity changes, as presented in equation (3.4) with an exponent n=0. Three simulations have been performed by A21, NRG and UDC using iCP, ORCHESTRA and CORE, respectively. The only difference between these models is that kinetically-controlled mineral phases were not included in the CORE model. However, as shown previously (comparison between P3 and FRC), similar results are expected. Figure 16 presents the results of this set together with FRC results for comparison purposes. As shown in the porosity distribution profiles, calcite precipitation

is predicted near the interface leading to a residual porosity value of 0.001. As the effective diffusion coefficient is coupled with porosity, its value is reduced linearly with porosity at that point (40 times reduction). Porosity clogging is predicted at 50,000 years (upper right plot in Figure 16), virtually stopping further concrete-clay interactions. As a consequence, changes in pH values are limited after 100,000 years (bottom left plot in Figure 16). On the COx side of the interface, pH remains under 7.2 in the entire domain. C-S-H dissolution in concrete is limited to 5 cm (bottom right plot in Figure 16). When compared to the FRC (black solid line in Figure 16), degradation in S1 is less extended even after 50,000 years. This difference increases with time, as interaction is almost stopped in this sensitivity case. When comparing results between codes, a different degradation profile is found for C-S-H gel in the results obtained with CORE. This may be related to the increase in porosity values found between x= 15 cm and x= 20 cm, that results in a high increase of effective diffusion coefficient in this region.

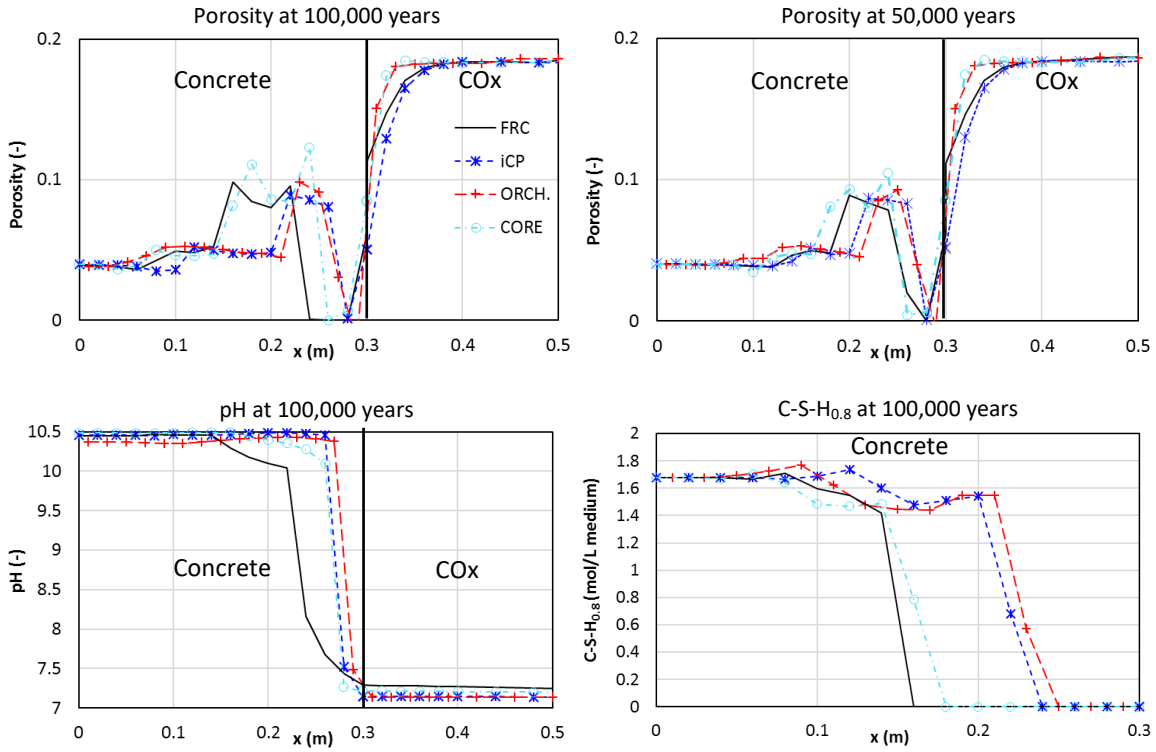

Figure 16. *Porosity (-), pH (-) and C-S-H gel (in mol/L medium) distribution profiles at 100,000 years. Results for FRC and models coupling linearly porosity (equation 3.4) with effective diffusion coefficient developed by A21, NRG and UDC (S1: porosity coupling).*

The last set of simulations concerning porosity coupling involves the cases including non-linear porosity-diffusion relations. Exponential porosity-diffusion laws with different exponents (equation 3.4) are grouped together with simulations including the expressions defined by equation (3.6) and equation (3.7). Figure 17 presents the results of all these simulations and compares with the FRC outcomes in terms of porosity and pH distribution profiles at 100,000 years. Overall, the results show that the closer to the interface the calcite precipitation peak is predicted, the lower the degradation is in terms of pH of the concrete porewater.

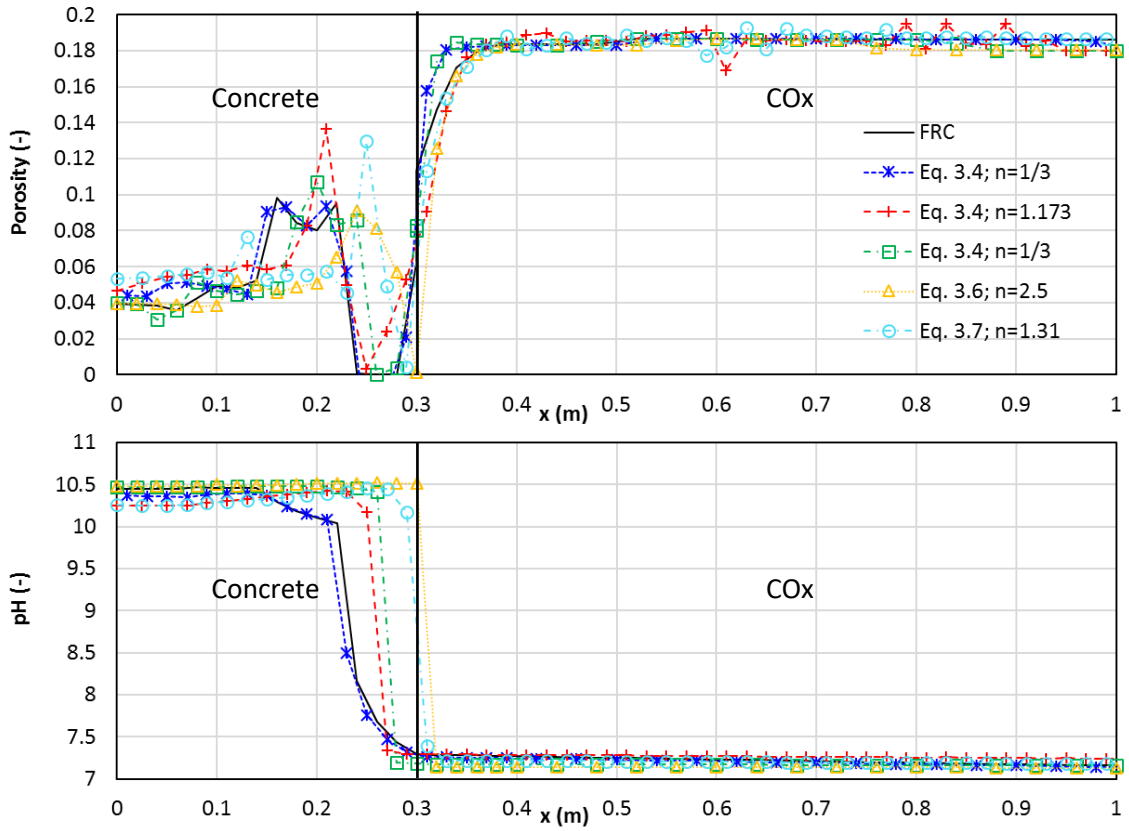

Figure 17. *Porosity (-) and pH (-) distribution profiles at 100,000 years. Results for FRC and models coupling porosity (equations 3.4 to 3.7) with effective diffusion coefficient developed in A21, NRG, JUELICH and UDC (S1: porosity coupling).*

4.6 S2: Lower diffusion in concrete

In this subsection, results for a less diffusive concrete material are presented. This simulation, performed by Andra and UDC using MIN3P and CORE, respectively, considers a constant effective diffusion coefficient of $1 \cdot 10^{-13}$ for the concrete barrier (one order of magnitude lower than for the FRC). This value is closer to those expected for this concrete mix with a low w/b ratio. Figure 18 shows the porosity, pH and mineralogical distribution profiles at 100,000 years and compared to those obtained in the FRC. First of all, the comparison of the results of S2 obtained with MIN3P and CORE show a very good agreement. The differences with the FRC are explained below. As expected, the level of alteration at a given time is much more limited in case S2. Porosity clogging is not reached even after 100,000 years, and changes are only noticeable over a distance of 10 cm from the interface. In the concrete barrier, pH values lower than 10.5 are only found close to the interface (4 cm), where the C-S-H gel dissolves. In turn, dolomite is not depleted at any point in the COx domain (although dissolution is found over 30 cm). Overall, the degradation process is qualitatively consistent with that of the FRC but with a much longer time scale.

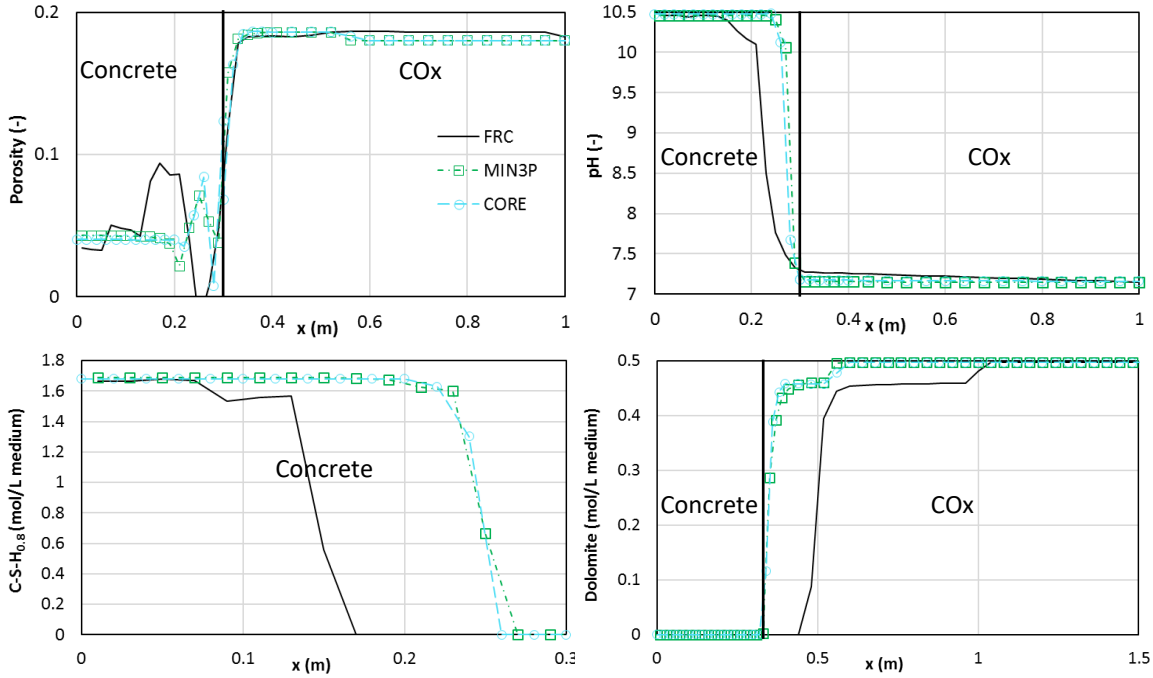

Figure 18. *Porosity (-), pH (-) and mineral concentration (mol/L medium) distribution profiles at 100,000 years. Results for S2 developed in Andra and UDC and FRC (S2: lower diffusion in concrete).*

4.7 S3: Multicomponent diffusion

In this subsection, results for a simulation case including multicomponent diffusion are presented. This simulation was performed by NRG with ORCHESTRA and considers an effective diffusion coefficient of $1 \cdot 10^{-12}$ for species without specific diffusion data (to be comparable to the FRC). Multicomponent diffusion is modelled using the Nernst-Plank equations (e.g. Galíndez and Molinero, 2010; Meeussen, 2019). With this approach, the diffusion coefficients of each species in free solution are needed (see Appendix C). These were extracted from the phreeqc.dat database of PHREEQC (Parkhurst and Appelo, 2013). In Figure 19, porosity and pH distribution profiles are presented at 100,000 years and compared to those obtained with ORCHESTRA for the FRC. Results in terms of porosity distribution show an increase of mineral precipitation and dissolution, with maximum porosity values that are higher than in the FRC, while minimum porosity is also lower. These changes in mineral volume contrast with the results in terms of pH values. The pH profile reflects less alteration in the concrete side after 100,000 years.

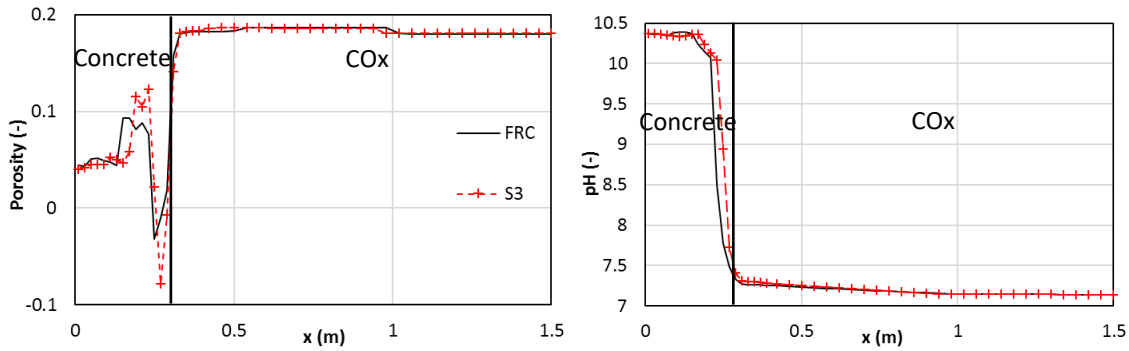

Figure 19. *Porosity (-) and pH (-) distribution profiles at 100,000 years. Results for S3 and FRC developed by NRG with ORCHESTRA (S3: multicomponent diffusion).*

4.8 S4: Different thermodynamic database

This sensitivity case considers the addition of supplementary thermodynamic data to the ThermoChimie v9b0 (Giffaut et al., 2014) database used in the full reference case. The simulation has been performed by KIT using iCP. Results after 100,000 years are compared to the FRC (FRC results obtained using iCP in this case). Figure 20 presents the distribution profiles for pH and ionic strength. Results show very good agreement in terms of pH or ionic strength of the pore solution (to be noted that this latter variable is very sensitive to chemical changes).

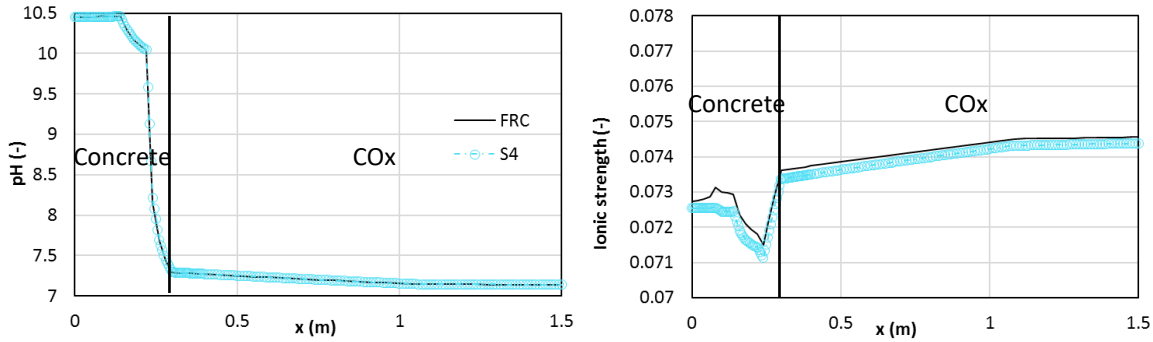

Figure 20. *Porosity (-) and ionic strength (-) distribution profiles at 100,000 years. Results for S4 and FRC developed by KIT with iCP (S4: different thermodynamic database).*

5 SUMMARY AND CONCLUSIONS

Within the CEBAMA project, one of the activities undertaken was to conduct a common modelling task for benchmarking reactive transport tools used in the project. The Modelling Task has served to build confidence on the representation of these complex systems with reactive transport tools when simulating the long-term behaviour of low-pH cementitious materials. The impact of keys parameters, such as diffusion coefficients, thermodynamic data, or couplings between geochemical and transport parameters, has also been assessed. The results show not only the high level of understanding of the governing processes but also the good agreement obtained with different codes, which is essential to demonstrate the applicability of these numerical tools to support the safety assessments.

Five reactive transport codes, namely iCP, ORCHESTRA, MIN3P, CORE, and OGS, have been compared using a methodology based on a set of simulations with increasing complexity. Overall, the results are in good agreement between the different codes. More than 30 reactive transport simulations were performed within the Modelling Task, with a thorough assessment of the influence of key variables and parameters. The main outcomes from the simulations are the following:

- Very good agreement between codes of the diffusion of a tracer in the concrete-clay system
- The effect of kinetically-controlled mineral phases in the clay is reduced in the present simulation, due in part to the low-pH porewater of concrete which has the effect of reducing the pH-dependent dissolution rates;
- Montmorillonite dissolution is negligible even near the interface after 100,000 years, which shows not only the effect of considering a low-pH concrete composition, but also of assuming a limited concrete volume;
- The effect of accounting for the coupling between mineral reactions and changes in porosity and diffusion coefficient is significant, especially in this case where calcite formation reduces substantially the porosity;
- A reduction of the effective diffusion coefficient of concrete from $1 \cdot 10^{-12}$ to $1 \cdot 10^{-13}$ m^2/s leads to a 50% reduction of the degradation extent;
- For the particular setup of the FRC, not accounting for the electrochemical coupling of multicomponent diffusion leads to a slightly larger decrease in pH of concrete porewater;
- The results of the FRC were not sensitive to the addition of other cementitious mineral phases in the thermodynamic database.

Thus, after 100,000 years of interaction, concrete degradation, characterized by C-S-H gel dissolution, is expected to be limited to the first 15 cm due to the low diffusion coefficient of concrete. On the clay side, 20 cm of dolomite dissolution is predicted, although other smaller changes in chemical composition are expected over a wider extent. Calcite precipitation is expected to eventually clog porosity, at a faster rate in the concrete side of the interface. Porosity clogging in the Full Reference Case is expected after around 30,000 years.

6 REFERENCES

Berner U., 2002. Project Opalinus Clay: Radionuclide concentration limits in the cementitious near-field of a ILW repository. PSI Bericht 02-26, Switzerland.

Bildstein O., Claret F., 2015. Stability of clay barriers under chemical perturbations. Chapter 5 - Stability of clay barriers under chemical perturbations, Eds.: C. Tournassat, C. I. Steefel, I. C. Bourg, F. Bergaya, In Developments in Clay Science, Elsevier, Vol. 6, 155-188.

Blanc P., Vieillard P., Gailhanou H., Gaboreau S., Gaucher E., Fialips C.I., Madé B., Giffaut E., 2015. A generalized model for predicting the thermodynamic properties of clay minerals. American Journal of Science, 315, 734-780.

Cochepin B., Trotignon L., Bildstein O., Steefel C. I., Lagneau V., van der Lee J., 2008. Approaches to modelling coupled flow and reaction in a 2D cementation experiment. Adv. Water Resour., 31(12), 1540-1551.

De Windt L., Marsal F., Tinseau E., Pellegrini D., 2008. Reactive transport modeling of geochemical interactions at a concrete/argillite interface, Tournemire site (France). Phys. Chem. Earth, 33, S295-S305.

Fernández R., Cuevas J., Mäder U. K., 2010. Modeling experimental results of diffusion of alkaline solutions through a compacted bentonite barrier. Cem. Concr. Res., 40, 1255-1264.

Galíndez J.M., Molinero J., 2010. On the relevance of electrochemical diffusion for the modeling of degradation of cementitious materials. Cem. Concr. Comp., 32(5), 351-359.

Gaucher E.C., Blanc P., 2006. Cement/clay interactions - a review: experiments, natural analogues, and modeling. Waste Manag. 26(7), 776-788.

Giffaut E., Grivé M., Blanc P., Vieillard P., Colàs E., Gailhanou H., Gaboreau S., Marty N., Madé B., Duro L., 2014. Andra thermodynamic database for performance assessment: ThermoChimie. Appl. Geochem., 49, 225-236.

Grandia F., Galíndez J.-M., Molinero J., Arcos D., 2010. Quantitative modelling of the degradation processes of cement grout. Project CEMMOD. SKB TR-10-25. Svensk Kärnbränslehantering AB.

Kosakowski G., Berner U., 2013. The evolution of clay rock/cement interfaces in a cementitious repository for low- and intermediate level radioactive waste. Phys. Chem. Earth, 64, 65-86.

Kosakowski G., Watanabe N., 2014. OpenGeoSys-Gem: A numerical tool for calculating geochemical and porosity changes in saturated and partially saturated media. Physics and Chemistry of the Earth, Parts A/B/C, 70-71, 138-149.

Kulik D.A., Wagner T., Dmytrieva S.V., Kosakowski G., Hingerl F.F., Chudnenko K.V., Berner U.R., 2013. GEM-Selektor geochemical modeling package: revised algorithm and GEMS3K numerical kernel for coupled simulation codes. Comput. Geosci., 17, 1-24.

Lehikoinen J., 2009. Bentonite-cement interaction – preliminary results from model calculations. POSIVA Oy Working Report 2009-37.

Liu S., Jacques D., Govaerts J., Wang L., 2014. Conceptual model analysis of interaction at a concrete-Boom Clay interface. Phys. Chem. Earth, 70-71, 150-159.

Lothenbach B., Winnefeld F., 2006. Thermodynamic modelling of the hydration of Portland cement. Cem. Concr. Res., 36(2), 209-226.

Lothenbach B., Matschei T., Möschner G., Glasser F., 2008a. Thermodynamic modelling of the effect of temperature on the hydration and porosity of Portland cement. Cem. Conc. Res., 38, 1-18.

Lothenbach B., Le Saout G., Gallucci E., Scrivener K., 2008b. Influence of limestone on the hydration of Portland cements. Cem. Conc. Res., 38, 848-860.

Marty N. M., Tournassat C., Burnol A., Giffaut E., Gaucher E. C., 2009. Influence of reaction kinetics and mesh refinement on the numerical modelling of concrete/clay interactions. J. Hydrol., 364, 58-72.

Marty N. M., Munier I., Gaucher E., Tournassat C., Gaboreau S., Vong C., Giffaut E., Cochepin B., Claret F., 2014. Simulation of Cement/clay interactions: feedback on the increasing complexity of modelling strategies. Transp. Porous Med., 104(2), 385-405.

Marty N.C., Bildstein O., Blanc P., Claret F., Cochepin B., Gaucher E.C., Jacques D., Lartigue J.E., Liu S., Mayer K.U., Meeussen J.C.L., Munier I., Pointeau I., Su D., Steefel C., 2015. Benchmarks for multicomponent reactive transport across a cement/clay interface. Comput. Geosci., 19(3), 635-653.

Mayer K.U., Frind E.O., Blowes D.W., 2002. Multicomponent reactive transport modeling in variably saturated porous media using a generalized formulation for kinetically controlled reactions. Water Resour. Res. 38, 1174.

Meeussen J.C.L., 2003. ORCHESTRA: An Object-Oriented Framework for Implementing Chemical Equilibrium Models. Environ. Sci. Technol., 37(6), 1175-1182.

Meeussen J.C.L., 2019. In Deliverable D3.06: Final results and interpretation of the modelling of experiments within CEBAMA, Edited by A. Idiart, CEBAMA.

Miller W. M., Alexander W. R., Chapman N. A., McKinley I. G., Smellie J. T., 2000. Geological disposal of radioactive wastes. Pergamon, The Netherlands.

Missana T., García-Gutiérrez M., Mingarro M., Alonso U., 2017. Analysis of barium retention mechanisms on calcium silicate hydrate phases. Cem. Concr. Res., 93, 8-16.

Mon A., Samper J., Montenegro L., Naves A., Fernández J., 2017. Long-term non-isothermal reactive transport model of compacted bentonite, concrete and corrosion products in a HLW repository in clay. J. Contam. Hydrol., 197, 1-16.

Nardi A., Idiart A., Trinchero P., de Vries L.M., Molinero J., 2014. Interface COMSOL-PHREEQC (iCP), an efficient numerical framework for the solution of coupled multiphysics and geochemistry. Computers & Geosciences 69, 10-21.

Olmeda J., Henocq P., Giffaut E., Grivé M., 2017. Modelling of chemical degradation of blended cement-based materials by leaching cycles with Callovo-Oxfordian porewater. Phys. Chem. Earth, 99, 110-120.

Palandri J.L., Kharaka Y.K., 2004. A Compilation of Rate Parameters of Water-Mineral Interactions Kinetics for Application to Geochemical Modeling. USGS-Report (2004-1068), Menlo Park, California, USA.

Parkhurst D.L., Kipp K.L., Charlton S.R., 2010. PHAST version 2: a program for simulating ground-water flow, solute transport, and multicomponent geochemical reactions. Techniques and Methods 6–A35, U.S. Geological Survey, Denver, Colorado.

Parkhurst D.L., Appelo, C.A.J., 2013. Description of input and examples for PHREEQC version 3 – A computer program for speciation, batch-reaction, one-dimensional transport, and inverse geochemical calculations. Techniques and Methods 6–A43, USGS, Denver, Colorado.

Parrot L.J., Killoh D.C., 1984. Prediction of cement hydration, Br. Ceram. Proc., 35, 41-53.

Roosz C., Vieillard P., Blanc P., Gaboreau S., Gailhanou H., Braithwaite D., Montouillout V., Denoyel R., Henocq P., Madé B., 2018. Thermodynamic properties of C-S-H, C-A-S-H and M-S-H phases: Results from direct measurements and predictive modelling. Appl. Geochem., 92, 140-156.

Samper J., Yang C., Zheng L., Montenegro L., Xu T., Dai Z., Zhang G., Lu C., Moreira S., 2011. CORE2D V4: A Code for Water Flow, Heat and Solute Transport, Geochemical Reactions, and Microbial Processes. Chapter 7 in Groundwater Reactive Transport Models, 160-185.

Savage D, Noy D J, Mihara M, 2002. Modelling the interaction of bentonite with hyperalkaline fluids. Appl. Geochem., 17, 207–223.

Savage D., Walker C., Arthur R., Rochelle C., Oda C., Takase H., 2007. Alteration of bentonite by hyperalkaline fluids: a review of the role of secondary minerals. Phys. Chem. Earth, 2, 287-297.

Savage D., 2011. A review of analogues of alkaline alteration with regard to long-term barrier performance. Mineral. Mag. 75(4), 2401-2418.

Sidborn M., Marsic N., Crawford J., Joyce S., Hartley L., Idiart A., de Vries L. M., Maia F., Molinero J., Svensson U., Vidstrand P., Alexander R., 2014. Potential alkaline conditions for deposition holes of a repository in Forsmark as a consequence of OPC grouting. SKB R-12-17, Svensk Kärnbränslehantering AB.

Schöler A., Winnefeld F., Ben Haha M., Lothenbach B., 2017. The effect of glass composition on the reactivity of synthetic glasses. J. Am. Ceram. Soc., 100, 2553-2567.

SKB, 2014. Initial state report for the safety assessment SR-PSU. Technical Report SKB TR-14-02, Svensk Kärnbränslehantering AB.

Soler J. M., 2013. Reactive transport modeling of concrete-clay interaction during 15 years at the Tournemire Underground Rock Laboratory. European Journal of Mineralogy, 25, 639–654.

Trotignon L., Peycelon H., Bourbon X., 2006. Comparison of performance of concrete barriers in a clayey geological medium. Phys. Chem. Earth, 31(10–14), 610-617.

Vasconcelos R., Walkley B., Hyatt N., Provis J., Corkhill C., 2018. The physico-chemical evolution of a low-pH cement in contact with groundwater. In: Proc. 2nd Annual Workshop of CEBAMA Project, 16-19 May 2017, Espoo, Finland. KIT scientific report (in press).

Vehmas T., Schnidler A., Löija M., Leivo M., Holt E., 2016. Reference mix design and castings for low-pH concrete for nuclear waste repositories. In: Proc. 1st Annual Workshop CEBAMA, Barcelona, Spain, May 2016.

Vehmas T., Leivo M., Holt E., Alonso M.C, García J.L., Fernández A., Isaacs M., Rastrick E., Read D., Vašíček R., Hloušek J., Hausmannová L., Večerník P., Červinka R., Havlová V., Lange S., Klinkenberg M., Bosbach D., Deissmann G., Montoya V., Ait Mouheb N., Adam C., Schild D., Schäfer T., 2018. Cebama reference mix design for low pH concrete and paste, preliminary investigations. In: Proc. 2nd Annual Workshop of CEBAMA Project, 16-19 May 2017, Espoo, Finland. KIT scientific report (in press).

Vopálka D., Rosendorf T., Štamberg K., Kittnerová J., Baborová L., 2019. Contribution of CTU/UJV to Deliverable D3.06: Final results and interpretation of the modelling of experiments within CEBAMA (Ed. A. Idiart).

Wagner T., Kulik D.A., Hingerl F.F., Dmytrieva S.V., 2012. GEMSelektor geochemical modeling package: TSolMod library and data interface for multicomponent phase models. Can. Mineral. 50, 1173-1195.

Watson C., Hane K., Savage D., Benbow S., Cuevas J., Fernández R., 2009. Reaction and diffusion of cementitious water in bentonite: results of 'blind' modelling. Applied Clay Science 45, 54–69.

7 APPENDIX A. Low-pH cement hydration modelling

AMPHOS 21 and PSI, in collaboration with Barbara Lothenbach from EMPA, have performed the concrete hydration modelling using PHREEQC v3 (Parkhurst and Appelo, 2013) and the Gibbs free energy minimization code GEMS v3 (Wagner et al., 2012; Kulik et al., 2013), respectively. The PHREEQC implementation used ThermoChimie v9b0 (Giffaut et al., 2014), consistent with the database to be used in the reference case. The GEMS implementation considered CEMDATA14, an updated version of the CEMDATA07 database (Lothenbach et al., 2008a), which has been studied as a sensitivity case in the hydration modelling exercise. To this end, the data set of the composition of the raw materials from the 1st Data Freezing (June 2017) has been used to define the stoichiometry of the clinker phases (alite, belite, aluminate and ferrite), silica fume (SF) and Blast Furnace Slag (BFS).

7.1 Input data

The composition of the CEBAMA reference concrete mix is detailed in Table 17. More details about the composition of the different mix components can be found in Vehmas et al. (2016, 2018).

Table 17. *Composition of CEBAMA reference concrete mix. Data from Vehmas et al. (2016, 2018). Density values from material manufacturers.*

Component	**Amount (kg/m^3_{conc})**	**Density (kg/m^3)**	**Volume fraction (-)**
CEM I 42.5	105	3100	0.0339
Silica fume	110	2300	0.0478
Blast furnace slag	65	2900	0.0224
Quartz filler	116	2650	0.0438
Aggregates			
0/1 mm	168	2600	0.0646
0/8 mm	770	2600	0.2962
8/16 mm	532	2600	0.2046
16/32 mm	396	2600	0.1523
Superplasticizer	16.8	1200	0.0140
Water	120	1000	0.1200
Total	2399		0.9996

The oxide composition of the CEM I 42.5 MH/SR/LA produced by CEMENTA AB (Anläggningscement) considered in the calculations is from SKB (2014), see Table 18. The oxide composition of silica fume (SF), from Finnsementti Oy and originating from Elkem, was measured by Univ. Surrey; while that of Blast Furnace Slag (BFS) by VTT.

Table 18. *Oxide composition of the components of the CEBAMA reference mix measured by different partners.*

Oxide	Mw (g/mol)	CEM I (wt. %)	SF (wt. %)	BFS (wt. %)
CaO	56.08	64	1.46	41.5
SiO_2	60.08	21	93.1	32.8
Al_2O_3	101.96	3.5	1.44	10.6
SO_3	80.06	2.2	0.47	1.4
MgO	40.30	0.7	0.88	8.29
Fe_2O_3	159.69	4.6	0.91	0.81
K_2O	94.20	0.62	1.73	0.62
Na_2O	61.98	0.07	-	0.62
CO_2	44.01	2.2	-	-
MnO	70.94	-	-	0.42
TiO_2	79.87	-	-	2.04
SrO	103.62	-	-	0.05
V_2O_5	181.88	-	-	0.09
ZrO_2	123.22	-	-	0.03
Total		98.89	99.99	99.27

To model the concrete hydration, the methodology developed by Lothenbach and Winnefeld (2006) and Lothenbach et al. (2008b), now widely used for different cementitious systems, is used. Cement hydration is assumed to occur under atmospheric conditions at 25°C and 100% relative humidity. It is based on coupling a set of kinetic reactions of dissolution of the mix components with thermodynamic calculations. The dissolution rates of the clinker phases (alite, belite, aluminate and ferrite) are taken from the empirical expressions proposed by Parrot and Killoh (1984). The dissolution rate of the blast furnace slag is taken from Schöler et al. (2017). The dissolution rates of the silica fume and the quartz filler considered here correspond both to that of quartz from Palandri and Kharaka (2004), which is a pH-dependent transition state theory (TST) formulation. The specific surface areas of the BFS, silica fume, and quartz filler are either specified directly by the providers or derived from particle size distribution from the providers. Apart from these kinetically-controlled reactions, all other chemical reactions are considered under thermodynamic equilibrium.

The aggregates are considered as chemically inert, the same as with the superplasticizer. The alkali uptake in C-S-H phases (Na^+ and K^+) is considered using a cation exchange model, with a CEC that depends on the C-S-H concentration and its Ca/Si ratio. On the other hand, aluminium and magnesium uptake in C-S-H is not considered in the simulations. Note that C-A-S-H or M-S-H phases are not included in any of the thermodynamic databases used in the hydration model.

7.2 Results

Only the results obtained with the PHREEQC implementation of the hydration modelling using ThermoChimie are presented here, which are more compatible for the setup of the reference case. As stated above, the PHREEQC calculations presented here consider 1 kg of water in the initial mix as a reference. Therefore, the rest of components of the mix is scaled accordingly. The results presented below are given in volume (litres).

The dissolution curves of the clinker and binder components and quartz filler as a function of time are shown in Figure 21 and Figure 22, respectively. As expected, a complete dissolution of the clinker phases occurs in a relatively fast manner (~ 100 days). The BFS also dissolves almost completely

during the first 100 days. On the other hand, silica fume dissolves fast at the beginning, but after 100 days the pH of the pore solution drops down and then remains constant due to the formation of C-S-H phases with Ca:Si ratio of 0.8 and therefore the dissolution of silica fume is significantly slowed down. Finally, the quartz does almost not react, and only very small amounts are dissolved, what is due to the lower surface area compared to silica fume (see Table 10).

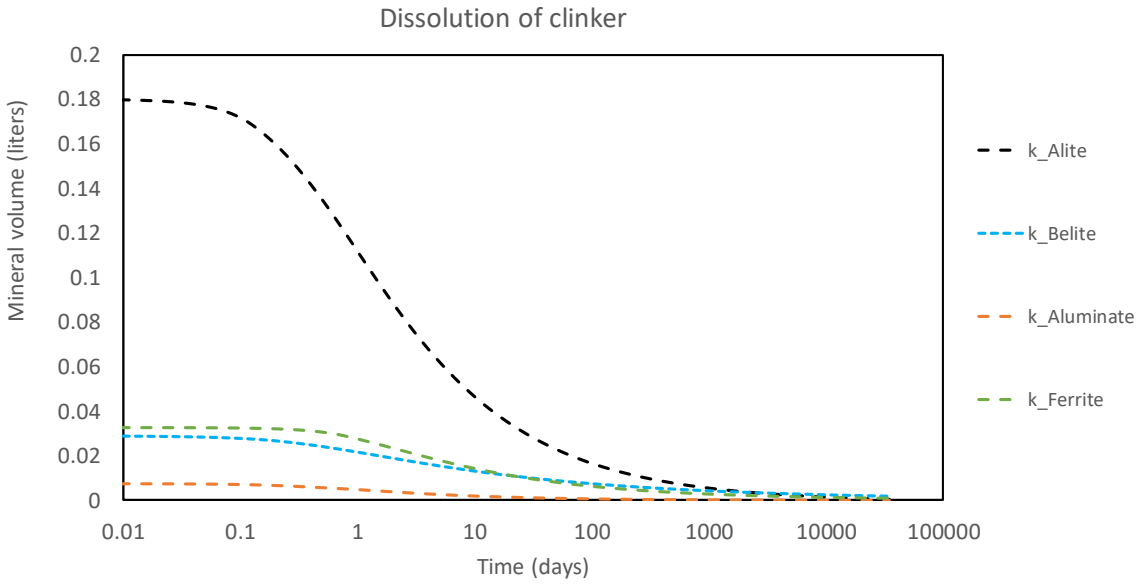

Figure 21. *Dissolution of the clinker phases as a function of hydration time.*

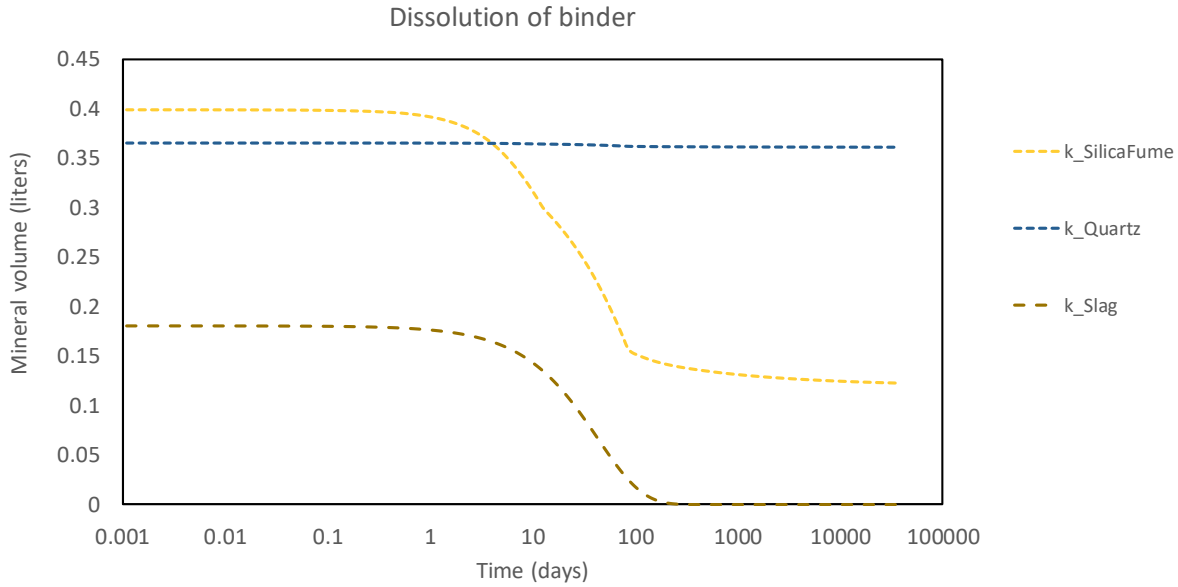

Figure 22. *Dissolution of blast furnace slag (k_Slag), quartz filler (k_Quartz), and silica fume (k_SilicaFume) as a function of hydration time.*

The evolution of the phase assemblage of the cement hydrates is shown in Figure 23 and Figure 24 (note different scales of vertical axes between the two figures). As hydration proceeds and silica is released from the binder, C-S-H phases form and gradually decalcify, ending up in a C-S-H with Ca:Si ratio of 0.8 as the main mineral phase (only three discrete C-S-H phases with Ca:Si ratio of 1.6, 1.2, and 0.8, are available in ThermoChimie). Other phases present after long hydration period (larger than 100 days) are ettringite, ferrihydrite, calcite, hydrotalcite, and strätlingite. Portlandite forms

during hydration but is destabilized due to the continuous release of Si from dissolution of the silica fume.

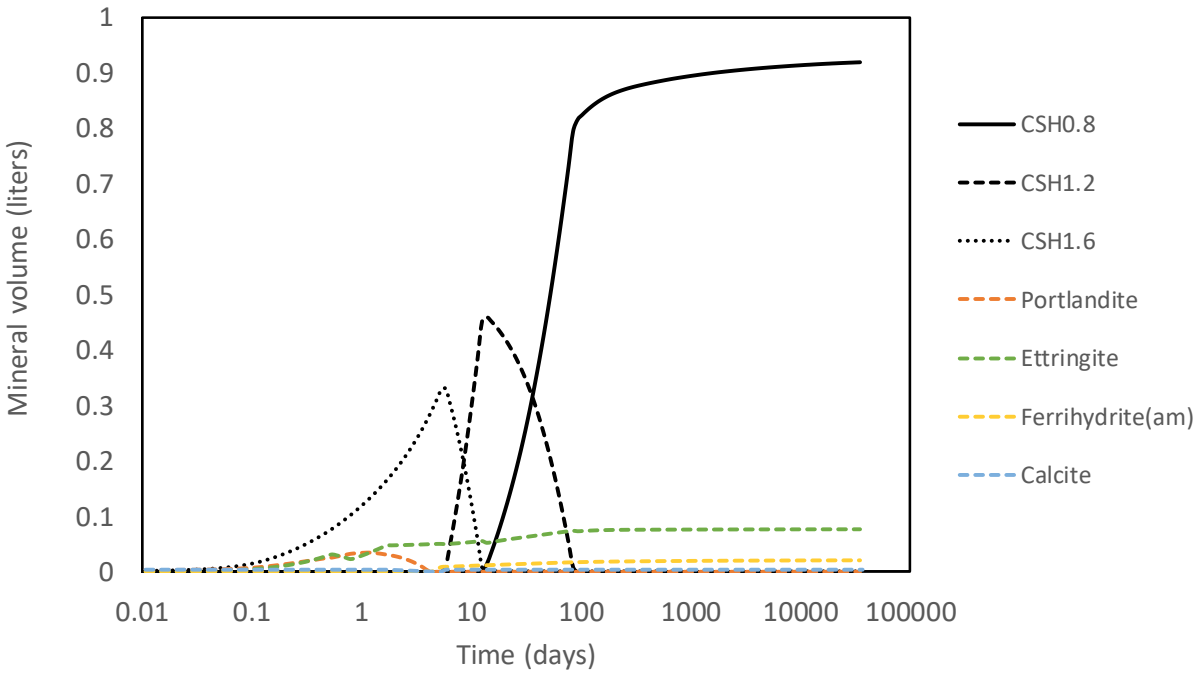

Figure 23. *Evolution of main cement hydrates as a function of hydration time.*

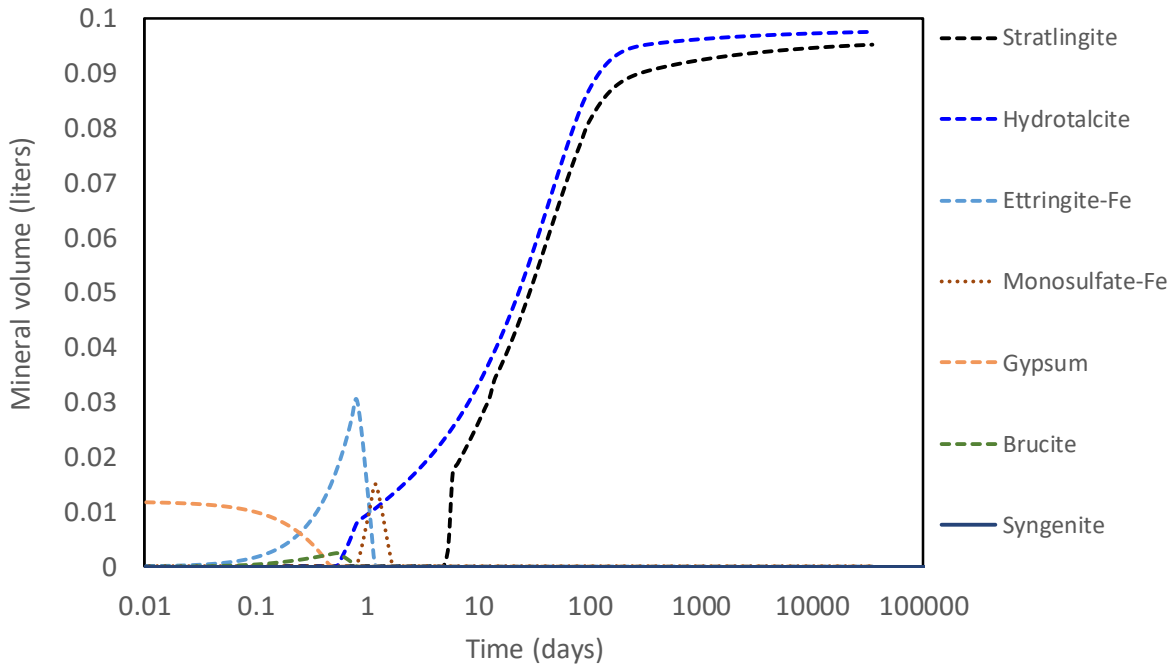

Figure 24. *Evolution of main cement hydrates as a function of hydration time.*

The evolution of porewater composition and pH is shown in Figure 25. The pH of the pore solution shows large variations from early hydration times, where it fluctuates between 12.5 and 13 at hydration times < 10 days, to pH ~10.7 at long hydration times. The evolution of the Ca:Si ratio of the C-S-H has a large impact on the pH of the pore solution once portlandite is dissolved. The largest pH decrease is observed when C-S-H transforms from CSH1.2 to CSH0.8. The alkali uptake (K^+ and

Na^+) in the C-S-H phases, modelled here using a cation exchange model, is also influenced by the pH of the solution. Mg^{2+} and Fe^{3+} concentration in the aqueous solution remains low (< 10^{-6} M) and controlled by the presence and the low solubility of hydrotalcite and ferrihydrite, respectively. Sulphate concentration remains below 3 10^{-2} M at all times, controlled by ettringite solubility. Aluminium concentration is in turn controlled by strätlingite solubility. At pH ≤ 10.7, the dissolution of silica fume and quartz filler is significantly lowered, and the system reaches a steady state close to equilibrium. Changes observed between hydration times of 10 years, 100 years or 1,000 years are very small.

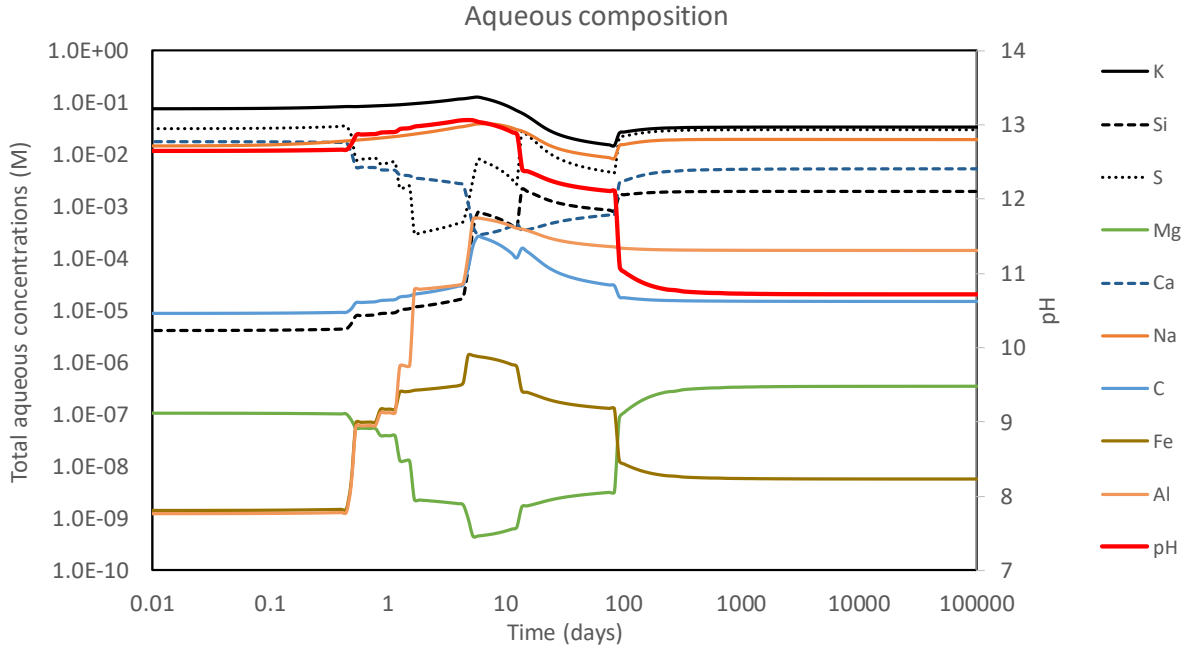

Figure 25. *Evolution of aqueous composition and pH as a function of hydration time.*

The total porosity and the amount of free water in the system as a function of hydration time is shown in Figure 26. Total porosity, denoted as ϕ_{tot}, is calculated with equation (A.1). The value of total porosity after long hydration times is around 0.063. This value is larger than which has been measured experimentally (Section 3.1) and therefore the initial porosity of concrete adopted in the Modelling Task is 0.04, between the modelled and the experimental values.

$$\phi_{tot} = \frac{V_{cem,0}+V_{water,0}-V_{cem,t}-V_{hydrates,t}}{V_{cem,0}+V_{water,0}+V_{aggr}+V_{sp}} \qquad \text{(A.1)}$$

In equation (A.1), *V* stands for volume (litre) and subscripts *cem*, *water*, *hydrates*, *aggr*, *sp*, and *inert* stand for unhydrated binder, water, cement hydrates, aggregates, superplasticizer (considered inert), and any chemically inert fraction. Subscripts *0* and *t* refer to initial values and values at time *t*.

Figure 26 also shows that the volume fraction of free water in the system is lower than porosity due to self-desiccation of the mix. This result is expected given the low water-to-binder ratio of the mix and the assumption that hydration takes place in a closed system, i.e. without an external source of water.

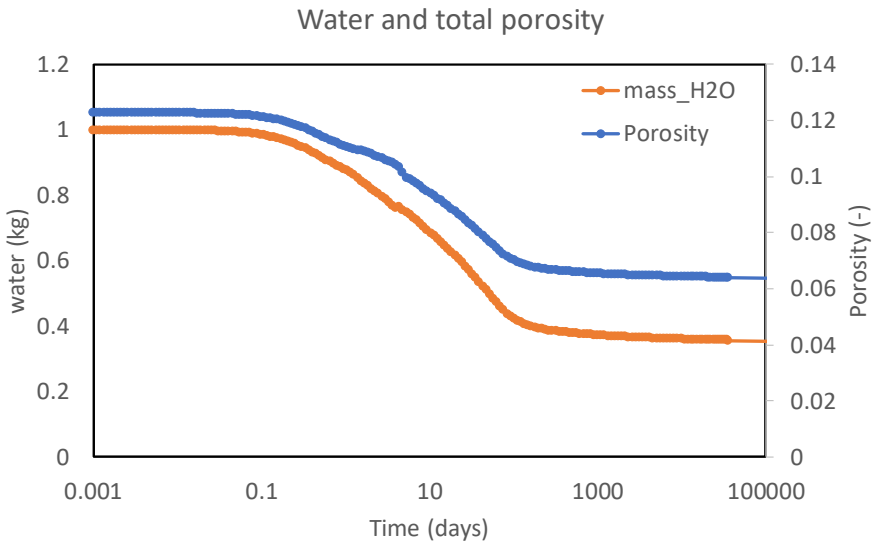

Figure 26. *Evolution of free water in the system and of total porosity as a function of hydration time.*

8 APPENDIX B. Elemental composition of concrete and clay domains

Table 19. *Elemental composition of the concrete domain, in mol/litre medium. The total chemical elements included in the porewater, cation exchanger, and minerals in equilibrium, are presented together. Additionally, the total chemical elements included in the minerals that are kinetically controlled are presented separately.*

Elements	**Al**	**C**	**Ca**	**Cl**	**Fe**	**K**	**Mg**	**Na**	**S**	**Si**	**Sr**	**H**	**O**
Total in equilibrium	$2.1317\cdot10^{-1}$	$8.6446\cdot10^{-3}$	1.5377	$4.00\cdot10^{-12}$	$6.6384\cdot10^{-2}$	$4.5568\cdot10^{-2}$	$1.8734\cdot10^{-1}$	$1.4276\cdot10^{-2}$	$3.6791\cdot10^{-2}$	1.7282	$4.00\cdot10^{-12}$	7.8364	9.6300
Aqueous Species	$5.7920\cdot10^{-6}$	$6.0240\cdot10^{-7}$	$2.0948\cdot10^{-4}$	$4.00\cdot10^{-12}$	$2.1788\cdot10^{-9}$	$1.3680\cdot10^{-3}$	$1.4944\cdot10^{-8}$	$7.6400\cdot10^{-4}$	$1.2232\cdot10^{-3}$	$8.0840\cdot10^{-5}$	$4.00\cdot10^{-12}$	$4.1620\cdot10^{-4}$	$5.3246\cdot10^{-3}$
Solvent	0	0	0	0	0	0	0	0	0	0	0	4.4407	2.2203
Exchanger composition	0	0	$1.7780\cdot10^{-2}$	0	0	$4.4200\cdot10^{-2}$	0	$1.3512\cdot10^{-2}$	0	0	0	0	0
Equilibrium phases	$2.1317\cdot10^{-1}$	$8.6440\cdot10^{-3}$	1.5197	0	$6.6384\cdot10^{-2}$	0	$1.8734\cdot10^{-1}$	0	$3.5568\cdot10^{-2}$	1.7281	0	7.8360	9.6246
Total (with kinetic phases included)	$2.2222\cdot10^{-1}$	$8.6446\cdot10^{-3}$	1.5461	$4.00\cdot10^{-12}$	$7.0061\cdot10^{-2}$	$5.7395\cdot10^{-2}$	$1.9435\cdot10^{-1}$	$1.4276\cdot10^{-2}$	$3.6791\cdot10^{-2}$	3.9735	$4.00\cdot10^{-12}$	$1.2354\cdot10$	$1.6387\cdot10$
Alternative total kinetic phases included*	$2.1317\cdot10^{-1}$	$8.6446\cdot10^{-3}$	1.5377	$4.00\cdot10^{-12}$	$6.6384\cdot10^{-2}$	$4.5568\cdot10^{-2}$	$1.8734\cdot10^{-1}$	$1.4276\cdot10^{-2}$	$3.6791\cdot10^{-2}$	3.9735	$4.00\cdot10^{-12}$	$1.2277\cdot10$	$1.6341\cdot10$

*In this case Silica Fume is considered as SiO_2, instead of using the stoichiometry of silica fume determined experimentally, with a concentration of 0.496924 mol/L medium.

Table 20. *Elemental composition of the COx domain, in mol/litre medium. The total chemical elements included in the porewater, cation exchanger, and minerals in equilibrium, are presented together. Additionally, the total chemical elements included in the minerals that are kinetically controlled are presented separately.*

Elements	**Al**	**C**	**Ca**	**Cl**	**Fe**	**K**	**Mg**	**Na**	**S**	**Si**	**Sr**	**H**	**O**
Total in equilibrium	$1.5307 \cdot 10^{-8}$	6.23030	5.6216	$7.4160 \cdot 10^{-3}$	$3.8932 \cdot 10^{-1}$	$1.4222 \cdot 10^{-2}$	$5.5680 \cdot 10^{-1}$	$7.6824 \cdot 10^{-2}$	$5.0779 \cdot 10^{-1}$	$3.2400 \cdot 10^{-5}$	$1.2638 \cdot 10^{-1}$	$1.2634 \cdot 10^{-3}$	1.9196·10
Aqueous Species	$1.5307 \cdot 10^{-8}$	$6.8868 \cdot 10^{-4}$	$1.3682 \cdot 10^{-3}$	$7.4160 \cdot 10^{-3}$	$7.8318 \cdot 10^{-6}$	$9.1980 \cdot 10^{-5}$	$9.3366 \cdot 10^{-4}$	$7.2144 \cdot 10^{-3}$	$1.9944 \cdot 10^{-3}$	$3.2400 \cdot 10^{-5}$	$4.3740 \cdot 10^{-5}$	$1.2634 \cdot 10^{-3}$	$1.0352 \cdot 10^{-2}$
Solvent	0	0	0	0	0	0	0	0	0	0	0	1.9983·10	9.9915
Exchanger composition	0	0	$8.5400 \cdot 10^{-2}$	0	$5.1450 \cdot 10^{-4}$	$1.4130 \cdot 10^{-2}$	$5.9070 \cdot 10^{-2}$	$6.9610 \cdot 10^{-2}$	0	0	$2.1390 \cdot 10^{-3}$	0	0
Equilibrium phases	0	6.2296	5.5348	0	$3.8880 \cdot 10^{-1}$	0	$4.9680 \cdot 10^{-1}$	0	$5.0580 \cdot 10^{-1}$	0	$1.2420 \cdot 10^{-1}$		1.9186·10
Total (with kinetic phases included)	5.2063	6.2303	5.7065	$7.4160 \cdot 10^{-3}$	1.2604	1.7380	1.4110	$1.6212 \cdot 10^{-1}$	$5.0779 \cdot 10^{-1}$	1.8635·10	$1.2638 \cdot 10^{-1}$	2.5442·10	8.0001·10

9 APPENDIX C

Table 21. *Diffusion coefficients in free solution for each ion used in the case S3 that considers multi-component diffusion with Nernst-Planck equations.*

Ion	D0 (m^2/s)	Ion	D0 (m^2/s)	Ion	D0 (m^2/s)	Ion	D0 (m^2/s)	Ion	D0 (m^2/s)
Al+3	5.59E-10	Cl2	2.00E-09	FeCl2+	2.00E-09	Mg[HCO3]+	4.78E-10	Si2O3[OH]4-2	2.00E-09
Ca+2	7.93E-10	ClO4-	2.00E-09	FeCl3	2.00E-09	Mg[OH]+	2.00E-09	Si3O5[OH]5-3	2.00E-09
Cl-	2.03E-09	CO	2.00E-09	FeCl3-	2.00E-09	Mg[S2O3]	2.00E-09	Si3O6[OH]3-3	2.00E-09
CO3-2	9.55E-10	CO2	1.92E-09	FeCl4-	2.00E-09	Mg[SO4]	4.45E-10	Si4O6[OH]6-2	2.00E-09
Fe+3	7.19E-10	Fe[CO3]	2.00E-09	FeCO3OH	2.00E-09	Mg4[OH]4+4	2.00E-09	Si4O7[OH]6-4	2.00E-09
H+	9.31E-09	Fe[CO3]2-2	2.00E-09	FeCO3OH-	2.00E-09	MgCl+	2.00E-09	Si4O8[OH]4-4	2.00E-09
H2	5.13E-09	Fe[CO3]3-3	2.00E-09	FeHCO3+	2.00E-09	Na[CO3]-	1.20E-09	Si6O15-6	2.00E-09
H4SiO4	1.10E-09	Fe[H3SiO4]+2	2.00E-09	FeHSO4+2	2.00E-09	Na[HCO3]	6.73E-10	SO2	2.00E-09
K+	1.96E-09	Fe[HS]+	2.00E-09	H[S2O3]-	2.00E-09	Na[OH]	2.00E-09	SO3-2	2.00E-09
Mg+2	7.05E-10	Fe[HS]2	2.00E-09	H[SO3]-	2.00E-09	Na[S2O3]-	2.00E-09	Sr[CO3]	2.00E-09
Na+	1.33E-09	Fe[HSO4]+	2.00E-09	H[SO4]-	1.33E-09	Na[SO4]-	1.33E-09	Sr[HCO3]+	2.00E-09
SO4-2	1.07E-09	Fe[OH]+	2.00E-09	H2[S2O3]	2.00E-09	NaAl[OH]4	2.00E-09	Sr[OH]+	2.00E-09
Sr+2	7.94E-10	Fe[OH]+2	2.00E-09	H2[SiO4]-2	2.00E-09	NaCl	2.00E-09	Sr[S2O3]	2.00E-09
Al[OH]+2	2.00E-09	Fe[OH]2	2.00E-09	H2[SO3]	2.00E-09	O2	2.35E-09	Sr[SO4]	2.00E-09
Al[OH]2+	2.00E-09	Fe[OH]2+	2.00E-09	H2S	2.10E-09	OH-	5.27E-09	SrCl+	2.00E-09
Al[OH]3	2.00E-09	Fe[OH]3	2.00E-09	H2S2O4	2.00E-09	S-2	7.31E-10		
Al[OH]4-	2.00E-09	Fe[OH]3-	2.00E-09	H3[SiO4]-	2.00E-09	S2-2	2.00E-09		
Al[SO4]+	2.00E-09	Fe[OH]4-	2.00E-09	HCl	2.00E-09	S2O3-2	2.00E-09		
AlH3SiO4+2	2.00E-09	Fe[OH]4-2	2.00E-09	HCO3-	1.18E-09	S2O4-2	2.00E-09		
Ca[H3SiO4]+	2.00E-09	Fe[SO4]	2.00E-09	HS-	1.73E-09	S2O5-2	2.00E-09		
Ca[HCO3]+	5.06E-10	Fe[SO4]+	2.00E-09	HS2O4-	2.00E-09	S2O8-2	2.00E-09		
Ca[OH]+	2.00E-09	Fe[SO4]2-	2.00E-09	HSO5-	2.00E-09	S3-2	2.00E-09		
Ca[S2O3]	2.00E-09	Fe+2	2.00E-09	K[OH]	2.00E-09	S3O6-2	2.00E-09		
Ca[SO4]	4.71E-10	Fe2[OH]2+4	2.00E-09	K[SO4]-	1.50E-09	S4-2	2.00E-09		
CaCl+	2.00E-09	Fe3[OH]4+5	2.00E-09	KAl[OH]4	2.00E-09	S4O6-2	2.00E-09		
CaCl2	2.00E-09	FeCl+	2.00E-09	KCl	2.00E-09	S5-2	2.00E-09		
CaCO3	4.46E-10	FeCl+2	2.00E-09	Mg[CO3]	4.21E-10	S5O6-2	2.00E-09		
CH4	1.85E-09	FeCl2	2.00E-09	Mg[H3SiO4]+	2.00E-09	Si2O2[OH]5-	2.00E-09		